ELECTRONIC STRUCTURE OF V_2O_5 POLYMORPHS AND $M_xV_2O_5$ BRONZES

A Thesis

by

CAROL MICHELLE LY

Submitted to the Office of Graduate and Professional Studies of
Texas A&M University
in partial fulfillment of the requirements for the degree of

MASTER OF SCIENCE

Chair of Committee,	Sarbajit Banerjee
Committee Members,	Matthew Sheldon
	Joseph H. Ross Jr.
Head of Department,	Simon North

December 2018

Major Subject: Chemistry

ABSTRACT

The energy landscape of vanadium oxide (V_2O_5) showcases a rich abundance of energetically proximate minima representing different metastable phases. In addition to the multiple polymorphs of V_2O_5, the open-framework structures can accommodate varying concentrations of metal ions within their structure to form mixed-metal oxide bronzes with the formula $M_xV_2O_5$. The bonding motif of each polymorph is determined by the connectivity of V—O bonds as well as the different inserted metal ions (M) and their stoichiometry (x); these materials thus serve as an excellent sandbox for elucidating structure—function correlations. The crystal structures of these semiconductors affect the electronic structure. Both the atomistic structure as well as the electronic structure determine the utility of these materials in applications such as energy storage and switchable devices. An electronic structure property of utmost importance to functional applications is the band gap. The study here uses diffuse reflectance spectroscopy paired with Kubelka-Munk analysis to determine the band gaps of well-characterized powders of these materials.

The discovery of new cathode materials that can intercalate cations and allow for both ionic and electronic transport is an urgent imperative for electrochemical energy storage. Materials with smaller band gaps tend to be better potential candidates than those with large band gaps owing to their better electronic conductivities and better ability to diffuse polarons. The band gaps of each polymorph of V_2O_5 are compared to evaluate the extent of covalent hybridization.

The deduced band gaps of polymorphs of V_2O_5 are furthermore of importance for energy harvesting. By synthesizing heterostructures of V_2O_5 and II-VI quantum dots, type-II charge-separated interfaces can be constructed and the separated carriers can be utilized for photocatalytic

reactions. The charge separation depends sensitively on the energetic offsets between the two semiconductors.

In addition, the mixed metal-oxide bronzes studied here exhibit metal-insulator transitions dependent on the concentration of metal-ions present. Trends in band gap values with the changes in metal cation content shows the strong correlation of structure and application.

ACKNOWLEDGEMENTS

I would like to thank my committee chair, Dr. Banerjee, and my committee members, Dr. Sheldon, and Dr. Ross, for their guidance and support throughout the course of this research. Dr. Banerjee provided inspiring support and advice as needed with great patience, and for that I am appreciative.

I would also like to thank my friends and colleagues and the department faculty and staff for making my time at Texas A&M University a great experience. I would like to thank my labmates in the Banerjee lab group for offering multiple views of the world to enrich my life. Specifically, I wish to thank Justin L. Andrews and Junsang Cho for their academic support during times of need and stress. Similarly, I wish to thank K. Malsha Udayakantha and S. Olivia Gunther.

Finally, I give thanks to my family, (mom, dad, Kevin, and Crystal) and Adrian Rosas for their unconditional encouragement and support.

CONTRIBUTORS AND FUNDING SOURCES

This work was supported by a thesis committee consisting of Professor(s) Sarbajit Banerjee and Matthew Sheldon of the Department of Chemistry and Professor Joseph H. Ross, Jr. of the Department of Physics.

Scanning electron microscopy image of bulk V_2O_5 in Chapter II was provided by Yuting Luo.

Density functional theory calculations of density of states in Chapter III was provided by Abhishek Parija.

The ICP-MS data analyzed for Chapter III was provided by Dr. Bryan Tomlin of the Elemental Analysis Lab of the Department of Chemistry's Center for Chemical Characterization and Analysis.

All other work conducted for the thesis was completed by the student independently.

NOMENCLATURE

DFT	Density Functional Theory
DOS	Density of States
DRS	Diffuse Reflectance Spectroscopy
HAXPES	Hard X-ray Photoemission Spectroscopy
ICP-MS	Inductively-Coupled Plasma-Mass Spectroscopy
MIT	Metal-Insulator Transitions
QD(s)	Quantum Dot(s)
SEM	Scanning Electron Microscopy
TA	Transient Absorption
XANES	X-ray Absorption Near-Edge Structure
XAS	X-ray Absorption Spectroscopy
XES	X-ray Emission Spectroscopy
XRD	X-ray Diffraction

TABLE OF CONTENTS

Page

ABSTRACT ii

ACKNOWLEDGEMENTS iv

CONTRIBUTORS AND FUNDING SOURCES v

NOMENCLATURE vi

TABLE OF CONTENTS vii

LIST OF FIGURES ix

CHAPTER I INTRODUCTION AND LITERATURE REVIEW 1

1.1 Metastable V_2O_5 Polymorphs 5
1.2 Mixed-Valence Ternary Vanadium Oxide Bronzes, $M_xV_2O_5$ 8
1.3 Optical Band Gap 10

CHAPTER II CORRELATING BONDING MOTIFS AND ELECTRONIC STRUCTURE OF STABLE AND METASTABLE V_2O_5 POLYMORPHS 16

2.1 Introduction to the V_2O_5 Polymorphs and Metastability 16
2.2 Synthetic Methods and Characterization of a Variety of V_2O_5 Polymorphs 18
2.2.1 Synthetic Methods 18
2.2.2 Structural Characterization and Band Gap Determination 20
2.3 Results and Discussion 20

CHAPTER III ALTERING *x* IN $Cu_xV_2O_5$ BRONZES TO MODIFY THE OPTICAL BAND GAP 29

3.1 Introduction 29
3.2 Synthesis and Characterization of Two-Phases of $Cu_xV_2O_5$ 32
3.2.1 Synthesis of β'- and ε-$Cu_xV_2O_5$ Bronzes 32
3.2.2 Removal of Cu from β'- and ε-$Cu_xV_2O_5$ Bronzes 33
3.2.3 Characterization 33
3.3 Results and Discussion 34

CHAPTER IV OUTLOOKS: SUMMARY AND CHALLENGES 42

4.1 Summary 42

4.2 Challenges 44

REFERENCES 45

LIST OF FIGURES

Page

Figure 1.1. Comparison of volumetric *vs.* gravimetric energy density for various battery technologies. Reprinted with permission from Ref. 1. 2

Figure 1.2. Dependence of band gap on size of quantum dots as a result of quantum confinement. 4

Figure 1.3. Energy landscape of energy *vs*. atomic displacement showing α-V_2O_5 at the minimum and ζ-V_2O_5, the metastable phase, in a local minimum. β-$Mg_xV_2O_5$ is shown as a material accessible from a metastable phase as opposed to the thermodynamically stable phase. Adapted and reprinted with permission from Ref. 14. 6

Figure 1.4. Several V_2O_5 polymorphs and $M_xV_2O_5$ bronzes that could be derived from the thermodynamic sink, α-V_2O_5. Reprinted with permission from Ref. 20. 7

Figure 1.5. Structural progression of $Li_xV_2O_5$ with increasing addition of Li-ions: (a) the orthorhombic phase of α-V_2O_5 (*Pmmn*), (b) puckered ε-phase (*Pmmn*), (c) increased puckered δ-phase (*Amma*), (d) full distorted γ-phase (*Pnma*). The Li- and V-ions are depicted as green spheres and red spheres, respectively, while O is in blue. Reprinted with permission from Ref. 17. 9

Figure 1.6. The structural difference between β- and β'-$M_xV_2O_5$ bronzes, where M occupies either β-sites (open circles, represented as A) or β'-sites (solid circles, represented as A'). The difference in distance between the M chains is shown on the right. Reprinted with permission from Ref. 24. 10

Figure 1.7. Plot of energy *vs.* wavevector for: (a) a free electron and (b) an electron in a monatomic linear lattice of lattice constant *a*. The E_g occurs at the first Brillouin zone, $k \pm \pi/a$. Reprinted with permission from Ref. 26. 11

Figure 1.8. (a) Crystal structure of orthorhombic α-V_2O_5. (b) First Brillouin zone of the simple orthorhombic lattice.[28] (c) Basic electronic band structure of orthorhombic V_2O_5 within the first Brillouin zone.[28] Energies are given relative to the valence-band maximum, E_v. Figure 1.8a reprinted with permission from Ref. 20. Figure 1.8(b-c) reprinted with permission from Ref. 28. 13

Figure 2.1. (a) The fundamental units of the V_2O_5 crystallographic system: [VO_5] square pyramids and distorted [VO_6] octahedral unit, where vanadium and oxygen atoms are represented by gray and red spheres, respectively, and the difference in shading indicates a shift in planes. Crystal structures of polymorphs of V_2O_5: (b) α-, (c) δ-, (d) γ'-, (e) β-, (f) ρ'-, (g) δ'-, (h) ε'-, and (i) ζ-phases of V_2O_5. Reprinted with permission from Ref. 19. 17

Figure 2.2. XRD patterns of polymorphs: bulk, α-, γ'-, and ζ-phase. 21

Figure 2.3. F(R) spectra *vs*. E for several polymorphs of V_2O_5. Linear trendlines extended to the x-intercept, where E_g is represented in eV. 23

Figure 2.4. SEM images of (a) bulk V_2O_5 and (b) hydrothermally grown α-V_2O_5 nanowires. Figure 2.4b reprinted with permission from Ref. 17. 24

Figure 2.5. (a) XES (left panel) and XAS (right panel) of α- and ζ-V_2O_5 nanowires with t_{2g} and e_g states labelled. (b) DOS of ζ-V_2O_5 (top) and α-V_2O_5 (bottom). (c) Band structure of α-V_2O_5 (left) and ζ-V_2O_5 (right). Reprinted with permission from Ref. 15. 25

Figure 2.6. The relative band alignment of polymorph V_2O_5/CdSe QDs. Reprinted with permission from Ref. 11. Manuscript in preparation. 27

Figure 3.1. Crystal structure of (left) β'-$Cu_{0.5}V_2O_5$ and (right) ε-CuV_2O_5, where the atoms Cu, V, and O atoms are colored blue, gray, and red, respectively. 30

Figure 3.2. (Left) DOS and (Right) projected DOS of β'-$Cu_xV_2O_5$ with various *x* stoichiometries calculated by DFT. Reprinted with permission from Ref. 37. Manuscript in preparation. 31

Figure 3.3. XRD patterns of β'-$Cu_xV_2O_5$ with varying Cu cation content. The corresponding colors of each material measured are to the right of the pattern. 35

Figure 3.4. Diffuse reflectance paired with Kubelka-Munk analysis for β'-$Cu_xV_2O_5$ with various amounts of Cu. The inset shows the E_g of each bronze deduced from this method *x*. 36

Figure 3.5. XRD patterns and powder images of the ε-$Cu_xV_2O_5$ set. Color changes occur for the as-prepared samples. 38

Figure 3.6. (a) Diffuse reflectance spectra of precursor ε-CuV_2O_5. (b) Band gap determination of ε-$Cu_xV_2O_5$. 39

CHAPTER I

INTRODUCTION AND LITERATURE REVIEW

Considerable research has focused on the development of renewable energy sources such as solar, wind, tidal, and geothermal energy to mitigate global reliance on fossil fuels, which are of limited abundance and are damaging to the environment.[1–3] However, renewable energy sources such as solar and wind are not always available during times of peak energy demand. To mitigate this issue, battery technologies provide a convenient way to store energy that has been harvested and produced during optimal conditions for a later time. Many current portable devices rely on Li-ion batteries as an energy storage system.[2] Li-ion batteries rely on the reversible insertion of Li-ions between a layered cathode material such as $LiCoO_2$ or $LiFePO_4$ and a carbon-based anode.[4] Such batteries have a long cycle life and provide safer working conditions as compared to using Li-metal as the anode.[2] However Li-ion batteries are characterized by lower theoretical volumetric and gravimetric energy densities as compared to their Li metal counterparts (Figure 1.1).[2] Li-ion batteries are also prone to catastrophic failure due to the formation of dendrites wherein Li metal plated on the anode grows with a needle- or fractal-like morphology, pierces the separator that separates the cathode and anode, and causes a short circuit.[5]

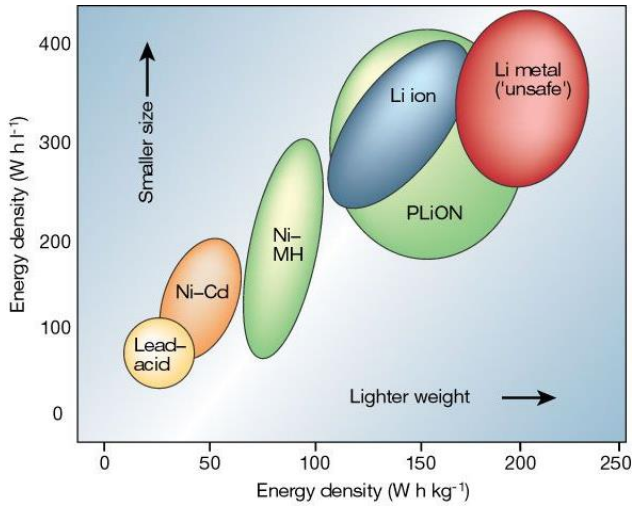

Figure 1.1. Comparison of volumetric *vs.* gravimetric energy density for various battery technologies. Reprinted with permission from Ref. 1.

Alternative metals such as Mg, Ca, and Al have been proposed as alternatives to unsafe, dendrite-forming Li-based anodes in batteries.[6,7] These metals provide benefits of increased theoretical energy densities owing to their divalent or trivalent nature: 3834, 2060, and 8046 mAh cm^{-3} for Mg, Ca, and Al, respectively, as compared to 840 mAh cm^{-3} for the graphite anode used in Li-ion batteries.[4,8] The ability to incorporate these metals in rechargeable, secondary batteries for energy storage requires the discovery of suitable cathode materials. These materials must possess the ability to intercalate and reversibly cycle divalent or trivalent cations while exhibiting higher charge density without substantial structural distortion and at reasonable rates.

As mentioned above, researchers are pushing toward using renewable energy sources to combat the potentially catastrophic effects of fossil fuels. In addition to energy storage, considerable recent attention has focused on energy harvesting. For solar energy exploitation, semiconductor-quantum dots have been studied as a tunable platform for light harvesting and charge transfer.[9–11] The energies of the valence and conduction band edges of semiconductors is

tunable a function of size, structure, and bonding motif.[9] The separation of the valence and conduction band in the electronic structure of a material represents the band gap, E_g. For quantum dots (QDs), the E_g and band-edge potentials are size-dependent due to quantum confinement, wherein below the characteristic Bohr radius of the material (typically < 10 nm), the electronic and optical properties differ from the bulk. The electronic structure varies from nanosized to bulk, even though they share the same unit cell and bond lengths.[12] The nanomaterial tends to have a large band gap as complete electron delocalization has not been achieved.[12] This inverse relationship between size and band gap (Figure 1.2) is summarized with the Brus' equation:

$$E_g^{nano} = E_g^{bulk} + \frac{\hbar^2 \pi^2}{8r^2}\left(\frac{1}{m_e^*} + \frac{1}{m_h^*}\right) - \frac{1.8e^2}{4\pi\varepsilon\varepsilon_0 r} \quad (1)$$

where r is the radius of the nanomaterial, m_e^* and m_h^* are the effective electron and hole masses, respectively, ε is the dielectric constant of the material, and ε_0 is the vacuum permittivity.[12] The second term relates to the particle-in-a-box concept as the electrons in the QDs are quantum confined as if they were particles in a box.[12] The third term represents the Coulomb interaction between electron-hole pairs.[12] Tunability of the size of these QDs allow for control over the optical, electronic, and magnetic properties of the material for possible applications for optoelectronics, photocatalysis, photovoltaics, and electrochemical energy storage.[9,11]

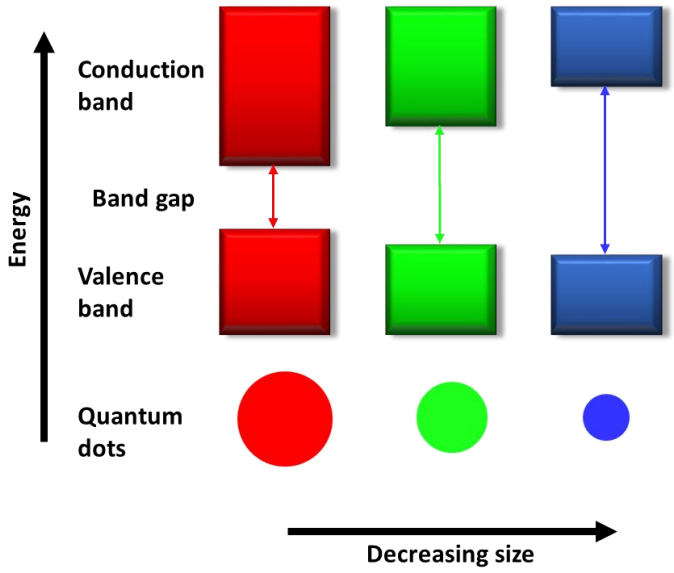

Figure 1.2. Dependence of band gap on size of quantum dots as a result of quantum confinement.

Although QDs have promise for use as the light harvesting element in photovoltaics or photocatalysis, their effective utilization is reliant on ultrafast charge transfer and the effective utilization of photogenerated electrons and holes in redox catalytic processes.[9,11] Obtaining greater efficiency requires either the increase of the amount of incident solar radiation available at a given time for absorption or the increase in charge separation efficiency. The latter can be controlled through chemical approaches, whereas the former depends on the condition of the day, which is beyond researchers' control.[11] Charge separation occurs when a photon is absorbed and an electron from the valence band is excited to the conduction band, leaving behind a positively-charged hole; transfer of either the electron or hole can give rise to a charge separated state within a heterostructure. Nanoscale heterostructures composed of distinct semiconductors provide tunability of the energetic positions of the valence and conduction band edges thus altering the light-harvesting, charge transfer, and catalytic processes.[9,13] The charge transfer process of these

heterostructures takes into account the charge separation of the electron-hole pair that forms during photoexcitation and their migration through the heterojunction. The charge separation and the charge transfer kinetics compete with the possible direct and indirect recombination processes of the electron-hole pair.[11] By tuning the interfaces of semiconductor heterostructures, recombination effects can be minimized.

Interfacial charge transfer across semiconductor heterojunctions gives rise to long-lived carriers that can be utilized to mediate redox catalysis processes necessary for solar energy conversion.[11] One strategy to increase carrier lifetimes involves the design and preparation of heterostructures of QDs with wide band gap metal oxide semiconductors. The compositional and size tunability of valence and conduction band edges of QDs paired with the compositional tunability of band edges in metal oxides provides control over the size and nature of the interface.[9,11,13] In such heterostructures, QDs act as light-harvesters (charge donors); the addition of metal oxides as charge acceptors enables tunability of energetic offsets and directionality of charge transfer.[11]

1.1 Metastable V_2O_5 Polymorphs

Vanadium oxide, V_2O_5, has been extensively explored as a result of the multiple distinctive polymorphs available for this composition, as a starting point for accessing variable vanadium redox states, the open frameworks adopted by most V_2O_5 polymorphs, and the reasonable voltage with respect to Li^+/Li. [1,10,14–19] These properties contribute to their potential for energy storage and photocatalytic or electrochromic applications.[1,10,14–20] On the free energy landscape of V_2O_5, multiple lower-energy wells exist in close proximity to one another (conceptualized as a “rugged”

energy landscape with scores of shallow wells).[19] The deepest well belongs to the most thermodynamically stable V_2O_5 phase, the α-phase, while the remaining wells are occupied by metastable phases of V_2O_5 (Figure 1.3). These metastable phases, known as polymorphs, all differ in atomic arrangements and bonding motif, which give rise to differences in electronic structure and function.[14,19] These metastable states arise from conditions and constraints such as temperature, pressure, surface confinement, tensile or compressive stress, and intercalation/deintercalation chemistry, just to name a few.[19]

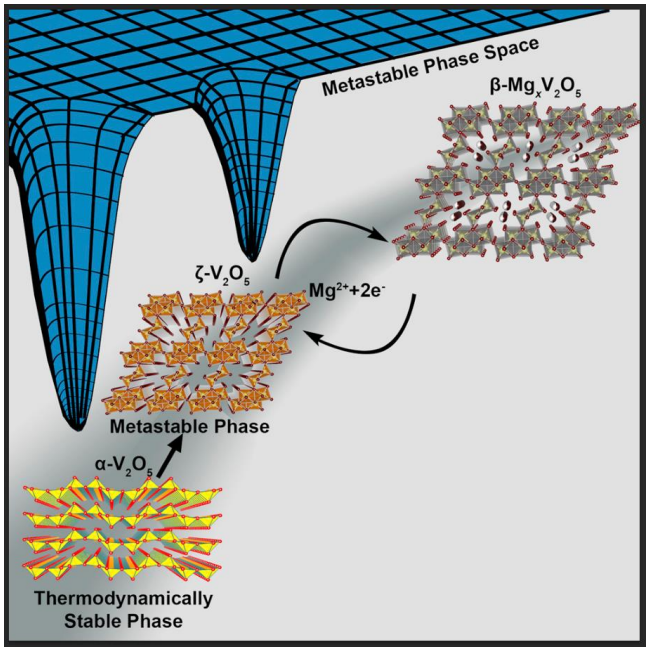

Figure 1.3. Energy landscape of energy *vs*. atomic displacement showing α-V_2O_5 at the minimum and ζ-V_2O_5, the metastable phase, in a local minimum. β-$Mg_xV_2O_5$ is shown as a material accessible from a metastable phase as opposed to the thermodynamically stable phase. Adapted and reprinted with permission from Ref. 14.

The α-phase is a well-studied intercalation host with an abundant number of intercalation sites, but its sluggish diffusion kinetics and intercalation-induced phase transitions that lead to

lattice distortions are a few of its shortcomings.[1,18] The application of the less stable polymorphs of V_2O_5 as cathode materials is not as well studied. Metastable V_2O_5 shows different crystal structures, ranging from distorted single layers, double layers, and tunnel-like structures, when compared to the single layered α-V_2O_5 (Figure 1.4).[20] The rich energy landscape of V_2O_5 materials provides many opportunities to explore the strong structure-function relationships that occur in each materials. The differences in crystal structure underpin the distinctive electronic structure characteristics of each polymorph. Possible applications of each polymorph, whether for energy storage or for extending charge separation in QD heterostructures are strongly dependent on the electronic structure.

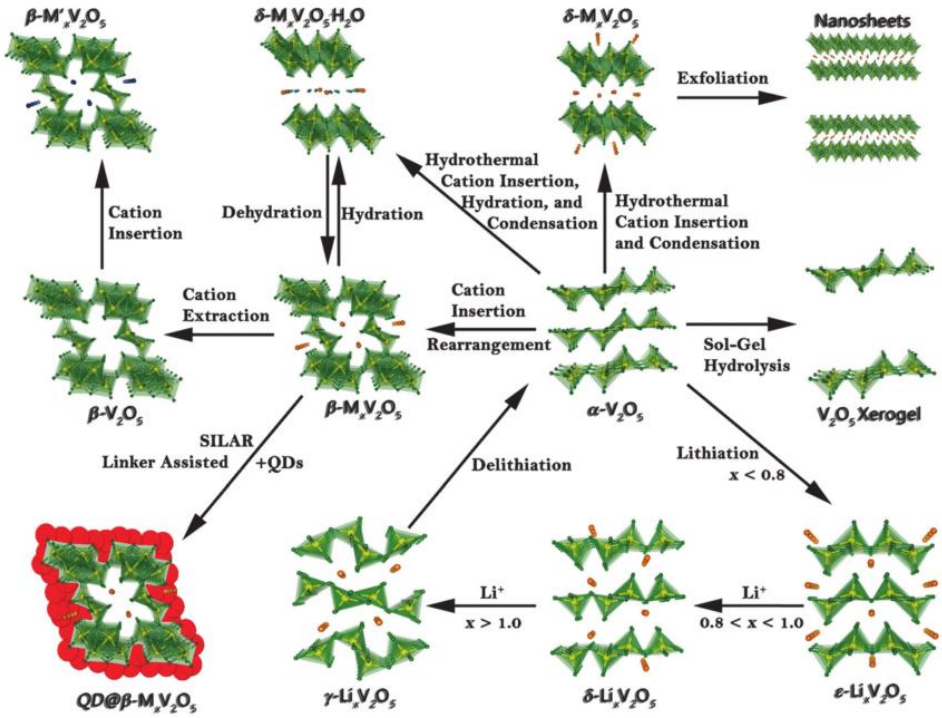

Figure 1.4. Several V_2O_5 polymorphs and $M_xV_2O_5$ bronzes that could be derived from the thermodynamic sink, α-V_2O_5. Reprinted with permission from Ref. 20.

1.2 Mixed-Valence Ternary Vanadium Oxide Bronzes, $M_xV_2O_5$

The versatility of the vanadium oxide class of materials does not stop at binary V_2O_5. Ternary vanadium oxide bronzes with chemical formula $M_xV_2O_5$ (where M is the intercalated metal cation in the vanadium oxide framework and *x* is the stoichiometry of the metal cation) are accessible from many synthetic approaches.[9,10,16,20–23] These bronzes showcase interesting behavior. Much like the V_2O_5 polymorphs discussed earlier, there are many structural phases for certain variations of metals and their stoichiometry. The phase of the V_2O_5 framework depends on the metal cation due to the differences in size, charge, and polarizability from one intercalant to the next.

A well-studied family of bronzes is that of $Li_xV_2O_5$, where Li^+ is chemically-intercalated into the single-layered V_2O_5 framework shown in Figure 1.5.[17] Reversible distortion occurs until the irreversible γ-phase is obtained at a Li content of $x \sim 1.0$ as seen in Figure 1.5.[17] The Li-content (*x*) influences the structural phase of the V_2O_5 framework: an α-phase is mostly retained when $x < 0.1$; a distorted ε-phase occurs for $0.35 < x < 0.8$; a puckered δ-phase is seen for $0.88 < x < 1.0$; and finally a strongly distorted, irreversible γ-phase arises for $x > 1.0$.[17]

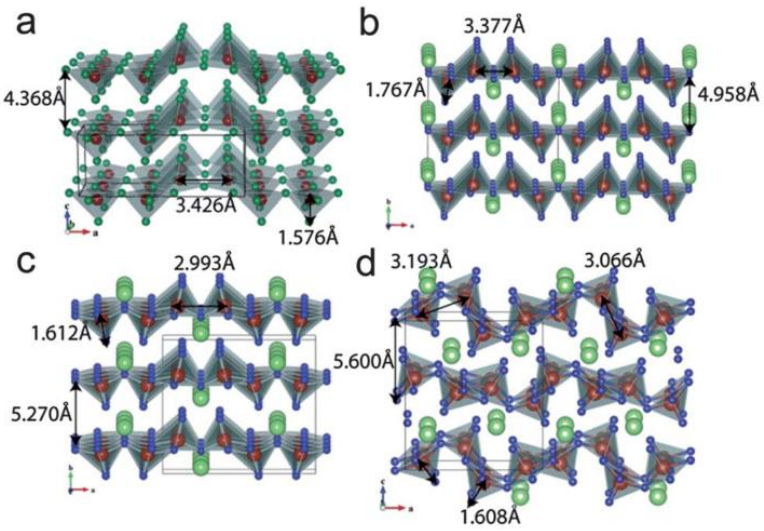

Figure 1.5. Structural progression of $Li_xV_2O_5$ with increasing addition of Li-ions: (a) the orthorhombic phase of α-V_2O_5 (*Pmmn*), (b) puckered ε-phase (*Pmmn*), (c) increased puckered δ-phase (*Amma*), (d) full distorted γ-phase (*Pnma*). The Li- and V-ions are depicted as green spheres and red spheres, respectively, while O is in blue. Reprinted with permission from Ref. 17.

The β/β'-phases of $M_xV_2O_5$ bronzes is analogous to ζ-V_2O_5 with their tunnel-like structures. The metal cations could occupy the β-sites or the β'-sites depending on the size of the cation. The smaller β'-sites are filled with either Li^+ or Cu^+ cations, with a space of 3.4 Å between the intercalated ions.[24] β-$M_xV_2O_5$ (M = Na^+, Ag^+, Ca^{2+}, etc.), on the other hand, depicts a spacing between the larger β-sites that is slightly smaller of 2.2 Å, as seen in Figure 1.6.[24] The availability of the two β/β'-sites within the tunnel framework showcases the variability of structures for $M_xV_2O_5$ materials. Because of the multiple avenues to alter the framework and bonding motifs of these ternary vanadium oxide bronzes, many unique properties can occur such as superconductivity, charge ordering, and metal-insulator transitions (MIT).[25] The tunability of each variable thus provides a means to control the properties and functions of the bronze.

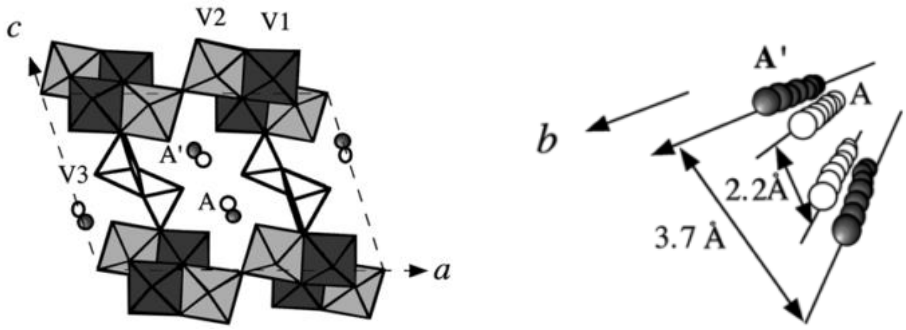

Figure 1.6. The structural difference between β- and β'-$M_xV_2O_5$ bronzes, where M occupies either β-sites (open circles, represented as A) or β'-sites (solid circles, represented as A'). The difference in distance between the M chains is shown on the right. Reprinted with permission from Ref. 24.

1.3 Optical Band Gap

The band gap, E_g, represents the separation between the top of the filled valence band and the bottom of the empty conduction band in a semiconductor as seen in the band structure. This property is important for semiconductors as it underpins some of their functions. The E_g is determined by the atomistic structure and bonding motif due to both of their influence on the electronic structure of the material. In turn, properties such carrier transport, optoelectronic, and electrochemical properties are affected, highlighting the importance of structure—function correlations for semiconducting materials.

Metals follow the free electron model, where electrons are not confined to just the valence band of the individual atoms. These valence electrons move freely throughout the metal at every energy state with a specific wavevector (k) value by becoming conduction electrons (Figure 1.7a).[26] On the other hand, the electrons in semiconductors and insulators experience confinement to specific energy states. The density of possible energy states at a given energy where electrons may exist are referred to as the density of states (DOS). Confinement of the electrons leads to only

specific energy states to be allowed. As seen in Figure 1.7b, the energy at k values of $\pm\pi/a$, where a is the lattice constant, are energetically forbidden.[26] The k values at the forbidden energy states are the Brillouin zone boundaries, and the electronically allowed spaces between these boundaries are known as Brillouin zones. Within the first region of k, electrons have their own allowed energy levels such that

$$E = \frac{\hbar^2 k^2}{2m} \tag{2}$$

where E is the energy level of the electron, $\hbar$ is the reduced Planck's constant and m is the effective mass of an electron. This energy diffract and distort near the Brillouin zone boundaries and gaps in energy, known as the forbidden band, occur at each forbidden energy values, as seen in a sample representation of an electronic band structure diagram in Figure 1.7b.[26] The energy difference of the forbidden band at the first Brillouin zone represents the E_g of the material.[26]

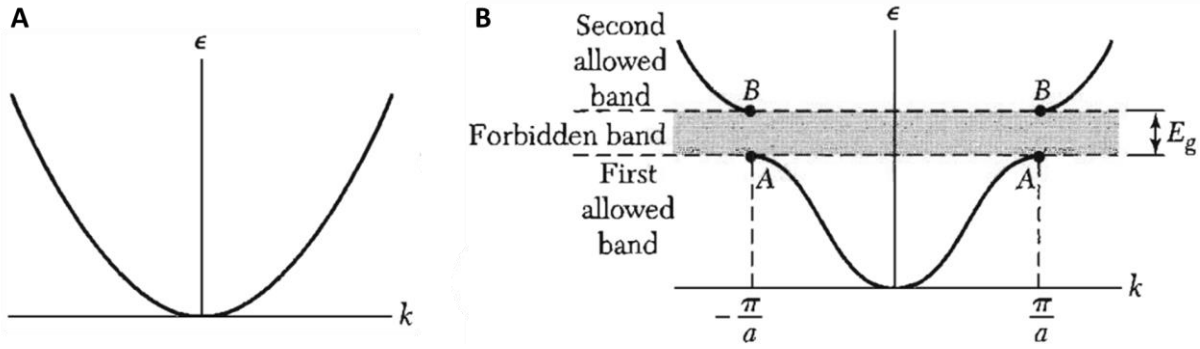

Figure 1.7. Plot of energy *vs.* wavevector for: (a) a free electron and (b) an electron in a monatomic linear lattice of lattice constant a. The E_g occurs at the first Brillouin zone, $k \pm \pi/a$. Reprinted with permission from Ref. 26.

There are two types of band gaps involved with semiconductors, the direct and indirect band gap. Direct band gaps occur in materials when the lowest point of the conduction band edge

is aligned with the highest point of the valence band at the same *k* value, while indirect band gaps occur when the two points occur at *k* values are different.[26,27] For a valence electron to be excited to the conduction band of direct band gap semiconductors, a quantum of light known as a photon with energy equal to the band gap must be absorbed. Exciting an electron in an indirect band gap material requires energy from both a photon and a quantum of vibrational energy known as a phonon.[26]

The band structure of materials can be calculated by computational methods utilizing density functional theory (DFT).[28] The structure of the thermodynamically stable, orthorhombic V_2O_5 (Figure 1.8a) shows chains of V-O polyhedra extended along the *a*-axis.[20] The DOS band diagram of V_2O_5 in Figure 1.8c shows the electronic states within the first Brillouin zone relative to *k*-space.[28]As seen along the Γ-*X* direction of the band structure, the dispersion of band energies is relatively less than the dispersion along Γ-*Y* and Γ-*Z*.[28] This reflects the anisotropies of the crystal structure as greater electron propagation is seen along Γ-*Y*, which is parallel to the chains in the *ab* planes.[28] With the band structure, the predicted E_g is ~1.74 eV.[28]

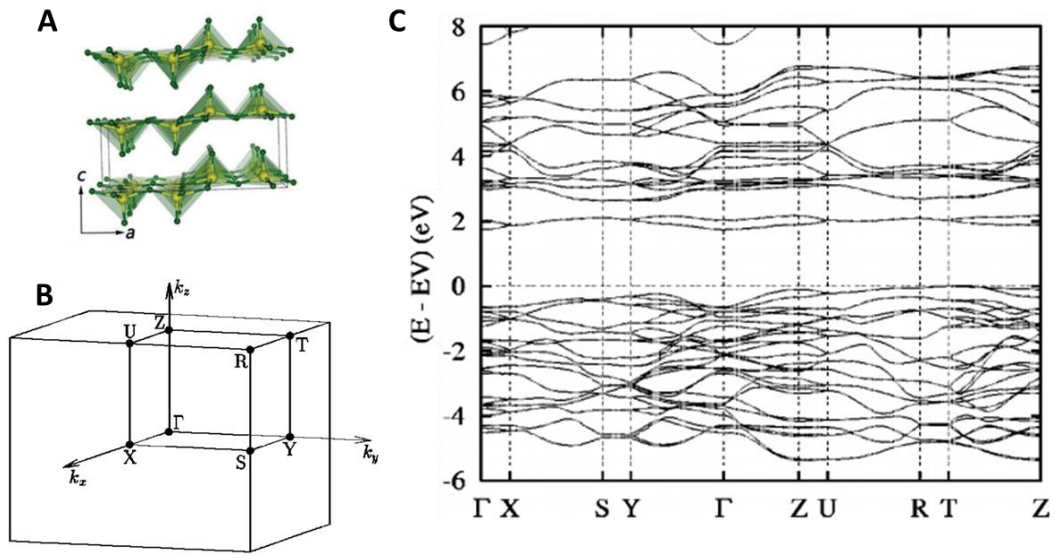

Figure 1.8. (a) Crystal structure of orthorhombic α-V_2O_5. (b) First Brillouin zone of the simple orthorhombic lattice.[28] (c) Basic electronic band structure of orthorhombic V_2O_5 within the first Brillouin zone.[28] Energies are given relative to the valence-band maximum, E_v. Figure 1.8a reprinted with permission from Ref. 20. Figure 1.8(b-c) reprinted with permission from Ref. 28.

DFT provides a predicted representation of the band structure of a material, allowing the E_g to be deduced. However, it is well-known that the predicted E_g values substantially (up to 40%) underestimate the experimental values.[29] This difference in calculated E_g to the experimental value arises from the difficulties for DFT to determine electron-correlation potential changes that occur discontinuously depending on the amount of electrons present.[29] Hybrid functionals allow for more accurate calculations of the bandgap but are often computationally prohibitive. However, experimentally determined E_g may be applied to DFT and provide a correction give a more accurate DOS.

To overcome the limitations of E_g prediction by DFT, a simple experimental method to determine the band gap of unsupported materials in powder form comes from utilizing diffuse reflectance spectroscopy (DRS) paired with Kubelka-Munk theory.[30] The band gap determined by

this method represents the optical band gap, E_{opt}, which is distinct from the fundamental band gap, E_g, mentioned earlier.[31] The optical band gap corresponds to the least amount of energy required for the lowest allowed electronic transition *via* absorption of a single photon.[31] Thus, this method yields values for allowed optical transitions while being mostly insensitive to transitions forbidden by selection rules that provide insight into phosphorescence or indirect band gaps. The E_{opt} is generally lower than E_g since the former considers the excited state where the electron-hole pair (exciton) remains electrostatically bound, whereas the latter considers the ionized state which requires additional energy to separate the electron-hole pair.[31] However, in inorganic semiconductor materials, the exciton binding energy is very small (a few meV) at room temperature that E_{opt} is similar to the fundamental E_g.[31] This allows the E_{opt} determined by DRS (denoted as E_g from here on) to be a good estimate of E_g for semiconductor materials.

In the UV-vis-NIR wavelength range, diffuse reflectance is measured as the amount of light reflection that is scattered off the surface of the material at many angles rather than at just one angle such as specular reflectance. DRS is used to determine electronic transitions of solids, in other words the E_g can be determined for semiconductor materials. Kubelka-Munk theory utilizes diffuse reflectance values to calculate E_g of highly light scattering materials and absorbing particles.[32] The Kubelka-Munk function is proportional to the absorption coefficient of the material and is related to diffuse reflectance, per:

$$F(R) = \frac{(1-R)^2}{2R} = \frac{K^*}{s} \quad (3)$$

where R is the measured diffuse reflectance at the respective wavelengths, $F(R)$ is the Kubelka-Munk function, K^* is the effective absorption coefficient, and s is the scattering coefficient. When $F(R)$ is plotted versus energy (eV) derived from the wavelength, E_g can be deduced from the x-

intercept of the linear portion of the plot. In other words, the energy onset when the material starts to attenuate light.

As such, my research thesis relies on the application of diffuse reflectance spectroscopy to determine the optical band gap of (i) several V_2O_5 polymorphs with varying V—O connectivity and (ii) several $M_xV_2O_5$ bronzes (M = Cu^+ with varying x). The E_g will provide insight in how electronic structure is modified as a function of V—O atomistic connectivity, the identity of the metal cation M, and its stoichiometry x. The diffuse reflectance results are interpreted with respect to first-principles DFT calculations and X-ray photoemission/X-ray absorption spectroscopy measurements.

CHAPTER II

CORRELATING BONDING MOTIFS AND ELECTRONIC STRUCTURE OF STABLE AND METASTABLE V_2O_5 POLYMORPHS

2.1 Introduction to the V_2O_5 Polymorphs and Metastability

The vanadium pentoxide (V_2O_5) family is a model system to understanding structure-function correlations due to it having a rugged energy landscape with several energetically similar bonding motifs, known as metastable polymorphs, occupying their respective energy wells, in addition to the thermodynamically stable phase.[1] The V—O connectivity and bonding strength varies from phase to phase of each V_2O_5 polymorph. As a result, the electronic structure, including the E_g, will vary with each phase, highlighting the importance of studying this family of materials in order to better understand structure—function correlations.[19,20]

There are six known synthesizable polymorphs of V_2O_5 comprised of [VO_5] square pyramids or a combination of the [VO_5] square pyramids and distorted [VO_6] octahedral units.[19] The thermodynamically stable α-phase of V_2O_5 comprises square pyramidally coordinated vanadium-centered, [VO_5], building blocks crystallized in the *Pmmn* space group with the corner- and edge-sharing polyhedra (Figure 2.1b).[10,11,25] In contrast, a metastable layered phase, γ'-V_2O_5 (*Pnma*), has [VO_5] building blocks, where the vanadium atom exists in two different crystallographic sites due to the expansion and distortion of the α-phase.[17,33] The transformation of α- to γ'-V_2O_5 (Figure 2.1(b-d)) can be conceptualized as resulting from changes of stacking and then puckering, α-V_2O_5 forms the δ- and then γ'-phase upon lithiation to Li-content of $x \sim 1$. Double-layered phases of V_2O_5, such as δ'- (*C2/m*) and ε'- (*C2/m*), are formed by distinct [VO_6] octahedral units connected as condensed V_4O_{10} double layers that are differently stacked as seen in Figure 2.1(g and h), where the degree of sliding in the crystallographic *a* direction differs.[8,16,19,34]

A metastable tunnel-like framework is also possible in the form of ζ-V_2O_5 (*C2/m*), where [VO_5] square pyramids connect layers of distorted [VO_6] octahedra perpendicularly.[10] In addition to those listed polymorphs, there are several other polymorphs of V_2O_5 (δ-, β-, and ρ'-V_2O_5) predicted by DFT to be structurally stable depicted in Figure 2.1(c, e, and f).[19] Given the different possible bonding motif that may occur in each polymorph of V_2O_5, the resulting electronic structure and energy band gap can be tuned. The abundant diversity of V_2O_5 polymorphs provides a toolbox full of structurally different materials that can be studied in terms of their electronic structures and possible applications such as in energy storage, photocatalysis, or electrochromic applications.

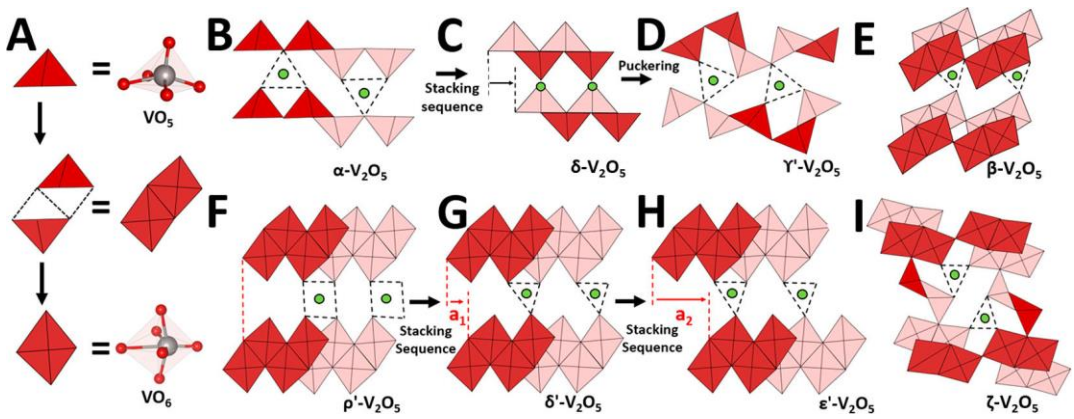

Figure 2.1. (a) The fundamental units of the V_2O_5 crystallographic system: [VO_5] square pyramids and distorted [VO_6] octahedral unit, where vanadium and oxygen atoms are represented by gray and red spheres, respectively, and the difference in shading indicates a shift in planes. Crystal structures of polymorphs of V_2O_5: (b) α-, (c) δ-, (d) γ'-, (e) β-, (f) ρ'-, (g) δ'-, (h) ε'-, and (i) ζ-phases of V_2O_5. Reprinted with permission from Ref. 19.

2.2 Synthetic Methods and Characterization of a Variety of V_2O_5 Polymorphs

2.2.1 Synthetic Methods

The synthesis of layered α-V_2O_5 nanowires was developed by our group.[17] In a 125 mL capacity Teflon-lined stainless-steel autoclave (Parr), ~1.60 g of V_2O_5 powder (Sigma-Aldrich), designated as the bulk sample, was reduced in a hydrothermal reaction at a temperature of 210°C for 3 days with ~ 0.46 g of $C_2H_2O_4$ (J.T. Baker) and 75 mL of water.[17] After 3 days, the autoclave was removed and allowed to cool to room temperature. This process yielded $V_3O_7{\cdot}H_2O$ nanowires in solution, which were filtered and washed with water and 2-propanol and then left to dry overnight. The resulting dried material was then in a muffle furnace at 350°C for 4 days, yielding α-V_2O_5 nanowires that were ground into a fine powder using a mortar and pestle for further characterization.[17]

As for γ'-V_2O_5, the synthesis took place in a glovebox under inert Ar atmosphere at room temperature. The synthesis started with the previously synthesized α-V_2O_5 nanowires (~1 g) mixed with 3 equivalences of LiI (~2.20 g), which was dissolved beforehand in just enough dry CH_3CN (ACN).[17] After dissolving the starting materials in the glovebox, the reaction was closed off to maintain the Ar atmosphere in the reaction flask and then removed from the glovebox to be stirred on a hot plate in ambient temperature. A color change occurred from orange to brown after constant stirring for 3 days. The brown solution was then filtered and washed with ACN and 2-propanol in ambient conditions. The solid (δ-$Li_xV_2O_5$) was allowed to dry overnight. After having been dried and ground into a fine powder using a mortar and pestle, δ-$Li_xV_2O_5$ was annealed in a tube furnace under Ar for 8 hours at 250°C. After 8 hours, the solid was allowed to dry, yielding γ-$Li_xV_2O_5$. The material was transferred back into the Ar-filled glovebox, where ~0.3 g of γ-$Li_xV_2O_5$ was introduced to ~0.23 g of $NOBF_4$ dissolved in ACN.[22] The reaction flask was sealed

and brought out of the glovebox to be stirred for 2-3 days. The color of the powder changed from blueish-black to green to yellowish-orange while stirring. At completion, the flask was opened under the fume and the solution yielded γ'-V_2O_5 after being filtered, washed, and dried. The dried material was ground using a mortar and pestle.

The final polymorph of interest, ζ-V_2O_5, was prepared utilizing the hydrothermal methods used in the synthesis of the thermodynamically stable α-V_2O_5, as outlined by Marley *et al.*[10] Stoichiometrically equivalent amounts of $AgCOOCH_3$ (~0.38 g, Sigma Aldrich) and bulk V_2O_5 (~1.25 g) were mixed with 87 mL of water in a 125 mL capacity Teflon-lined stainless-steel autoclave. After being sealed off, the autoclave was moved into a 210°C oven for 5-7 days. The autoclave was then removed and allowed to cool to room temperature, after which, the solution was vacuum filtered, washed with water and 2-propanol, and dried overnight to obtain β-$Ag_{0.33}V_2O_5$. The removal of Ag-ions from the β-sites required 0.80 mL 2 M HCl and 15 mL of H_2O to be introduced to ~0.300 g of β-$Ag_{0.33}V_2O_5$in a 23 mL capacity Teflon-lined stainless-steel autoclave. The autoclave was sealed and placed in a 210°C oven for 24 h as per:

$$\beta\text{-}Ag_{0.33}V_2O_5\ (s) + 0.29HCl\ (aq.) + 0.145O_2\ (g) \rightarrow$$
$$\zeta\text{-}Ag_{0.04}V_2O_5\ (s) + 0.29AgCl\ (s) + 0.145H_2O\ (l) \quad (4)$$

After completion, the autoclave was removed and allowed to cool to room temperature. The solution was filtered and washed with copious amounts of $Na_2S_2O_8$ to remove the AgCl impurity, water, and 2-propanol, as per:

$$0.29AgCl\ (s) + x Na_2S_2O_8\ (aq.) \rightarrow$$
$$x Na_2S_2O_8\ (aq.) + 0.145Ag_2S_2O_8\ (aq.) + 0.29NaCl\ (aq.) \quad (5)$$

where *x* represents an excess amount of $Na_2S_2O_8$ used. After washing, the material was dried overnight and the recovered ζ-V_2O_5 containing a small Ag^+ impurity was ground used a mortar and pestle.

2.2.2 Structural Characterization and Band Gap Determination

The dried product of each polymorph was ground using a mortar and pestle to obtain the material in powdered form. Powder X-ray diffraction data for structure determination for each polymorph of V_2O_5 were acquired in Bragg-Brentano geometry on a Bruker D8 Focus-Eco diffractometer with a Cu Kα radiation source (λ = 1.5418 Å). In order to determine the optical band gap, diffuse reflectance spectroscopy(DRS) paired with Kubelka-Munk theory was used.[27] Diffuse reflectance data were collected from 200 – 800 nm on a Hitachi U-4100 dual beam UV-vis-NIR spectrophotometer with the Praying Mantis™ attachment for powder samples.

2.3 Results and Discussion

The differences in crystal structure of each V_2O_5 polymorph are evident from powder X-ray diffraction (XRD) measurements. The XRD patterns show changes in the positions and intensities of each reflections, which corresponds to the changes in structure, as shown in Figure 2.2. The thermodynamic sink α-V_2O_5 crystallizes as a layered structure of orthorhombic *Pmmn* space group.[4] The structure consists of vanadium-centered [VO_5] square pyramid building blocks where the vanadium atom is double-bonded with an apical oxygen atom (denoted as the vanadyl oxygen) and single-bonded to four other oxygen atoms making up the base of the square pyramid.[4] The [VO_5] polyhedra share edges along the *a*-axis in an up-up-down-down formation and corner share along the *b*-axis to give rise to the sheet-like structure. These sheets are further stacked upon

each other and held together by van der Waals interactions to form the overall layered structure (Figure 2.1b).

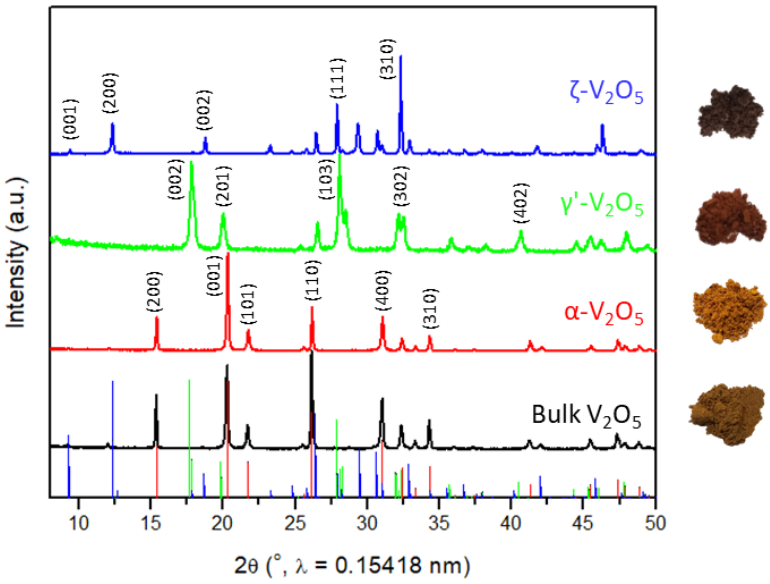

Figure 2.2. XRD patterns of polymorphs: bulk, α-, γ'-, and ζ-phase.

As α-V_2O_5 undergoes lithiation and delithiation, the V_2O_5 framework distorts and puckers to form γ'-V_2O_5. This metastable phase crystalizes in the *Pnma* space group where distorted square pyramids of [VO_5] form ribbons parallel to the *b*-axis through edge-sharing (Figure 2.1d).[22,33] The polyhedra corner share along the *a*-axis to form puckered layers. The stress that occurs with lithiation and delithiation of α-V_2O_5 yields the irreversible γ'-V_2O_5 with an increase in interlayer space from 4.37 Å to 5.02 Å.[22] The ζ-phase of V_2O_5 moves away from the single-layered structure made of [VO_5] polyhedra, as seen with α- and γ'-V_2O_5. The ζ-phase has three types of vanadium centers and crystalizes in the *C2/m* space group, as depicted in Figure 2.1i. Two different vanadium-centered distorted [VO_6] octahedra form edge-sharing chains along the *b*-axis with

corner-sharing connections along the *a*-axis.[18] The third type of vanadium center is in the form of [VO_5] square pyramids, which edge share along the *b*-axis, forming chains that connect the chains of edge-sharing octahedra along the *c*-direction.[18] Overall, the structure of ζ-V_2O_5 produces a tunnel-like structure that propagates along the *b*-axis that is accommodating to cation intercalation and diffusion.[18] These three phases are just several of the polymorphs of V_2O_5 that exist, where each polymorph contains variations of V—O bonding motifs and structures.

The differences in the crystal structures of the discussed polymorphs are expected to affect the respective electronic structures. In addition, the difference in color of each material (Figure 2.2), crudely corresponding to interactions with the visible region of the electromagnetic spectrum, confirms that there is a change in electronic structure. The orange color of α- and γ'-V_2O_5, where the latter is more orange, indicates a greater presence of V^{5+} in the form of the [VO_5] polyhedral building blocks.[10] As for the darker brown color of ζ-V_2O_5, the mixture of [VO_5] and [VO_6] polyhedra units gives rise to the mixed vanadium valence (V^{5+}/V^{4+}) in the polymorph leading to a less orange color for the material. The band gaps of each polymorph have been determined by extrapolating the linear regions of the Kubelka-Munk plots to the *x*-axis, as depicted in Figure 2.3. The band gaps of bulk, α-, γ'-, and ζ-V_2O_5 are 2.29, 2.31, 2.36, and 2.09 eV, respectively. Multiple diffuse reflectance scans (not provided here) were taken of each sample and the calculated E_g values are consistent across multiple replicates.

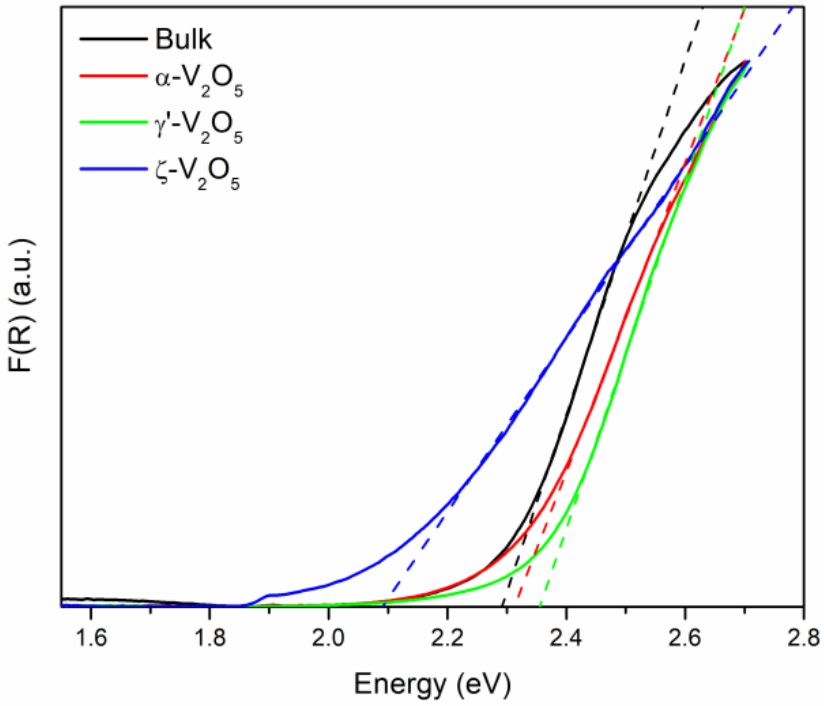

Figure 2.3. F(R) spectra *vs*. E for several polymorphs of V_2O_5. Linear trendlines extended to the x-intercept, where E_g is represented in eV.

The similarity in E_g of bulk and α-V_2O_5 verifies the practicality of using DRS with Kubelka-Munk theory for E_g determination. Bulk V_2O_5 is commercially available V_2O_5 in its thermodynamically stable α-phase. However, bulk V_2O_5 contains a mixture of solid, polycrystalline powders of different shapes and sizes ranging from tens to hundreds of micrometers.[17] The as prepared powdered α-V_2O_5 comprises of α-V_2O_5 with nanowire-like morphology. These nanowires are 150 – 250 nm in diameter and range several hundreds of micrometers in length.[17] The differences in size and shape of bulk V_2O_5 and α-V_2O_5 nanowires are seen in the SEM images in Figure 2.4. Although there is a three-fold reduction in size from bulk to α-V_2O_5 nanowires, the E_g remains relatively the same as α-V_2O_5 nanowires are not small enough to provoke quantum confinement effects to substantially increase the band gap when compared to

bulk V_2O_5. Both materials consist of V_2O_5 in its most stable phases, therefore E_g is expected to be similar.

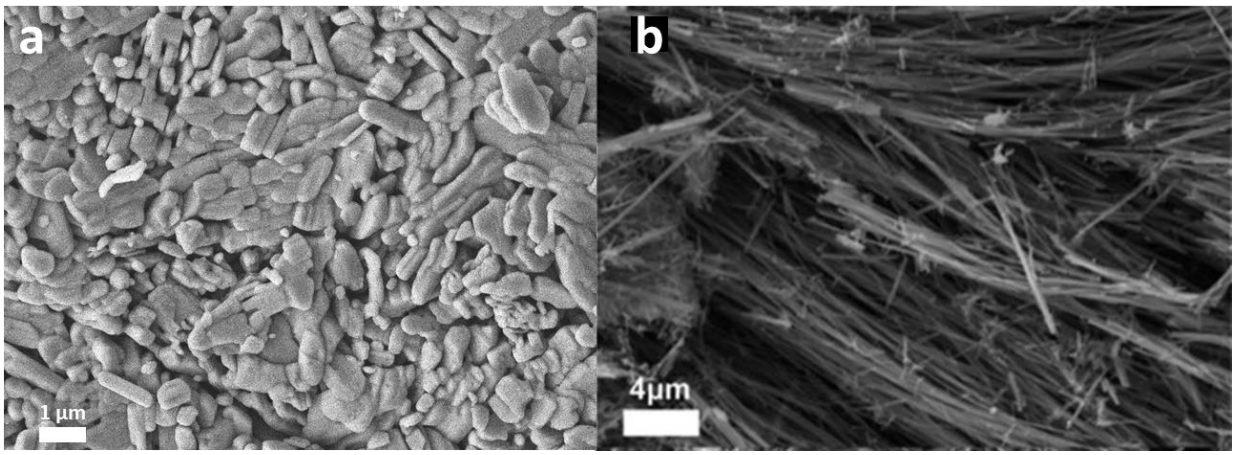

Figure 2.4. SEM images of (a) bulk V_2O_5 and (b) hydrothermally grown α-V_2O_5 nanowires. Figure 2.4b reprinted with permission from Ref. 17.

The previously reported band gaps of the α- and ζ-phase are 1.90 ± 0.20 and 1.50 ± 0.20 eV, respectively.[15] These values differ from the band gaps determined here by diffuse reflectance spectroscopy, which are 2.29 and 2.09 eV, respectively. The reported band gap of the two polymorphs as determined by Tolhurst *et al.* were estimated using X-ray emission and absorption spectroscopy (XES and XAS) (Figure 2.5a), which required a correction due to the core holes on the XAS spectra causing a shift in band gap to reflect an indirect band gap transition as opposed to the direct band gap determination by optical methods.[15] The core hole is created in XAS when the absorption of X-ray photon energy causes a core electron to be excited to an unoccupied state, resulting in a severe perturbation. The valence band is derived primarily from O 2p orbitals, whereas the conduction band is predominately V 3d in origin. For ζ-V_2O_5, the valence band

maximum is slightly higher in energy than α-V_2O_5, whereas the vanadium d-states in the conduction band edge is slightly lower in energy, leading to a reduction in the E_g (Figure 2.5c).[15] The reduction of the bandgap reflects the greater covalent hybridization of V 3d and O 2p states in the metastable polymorph.

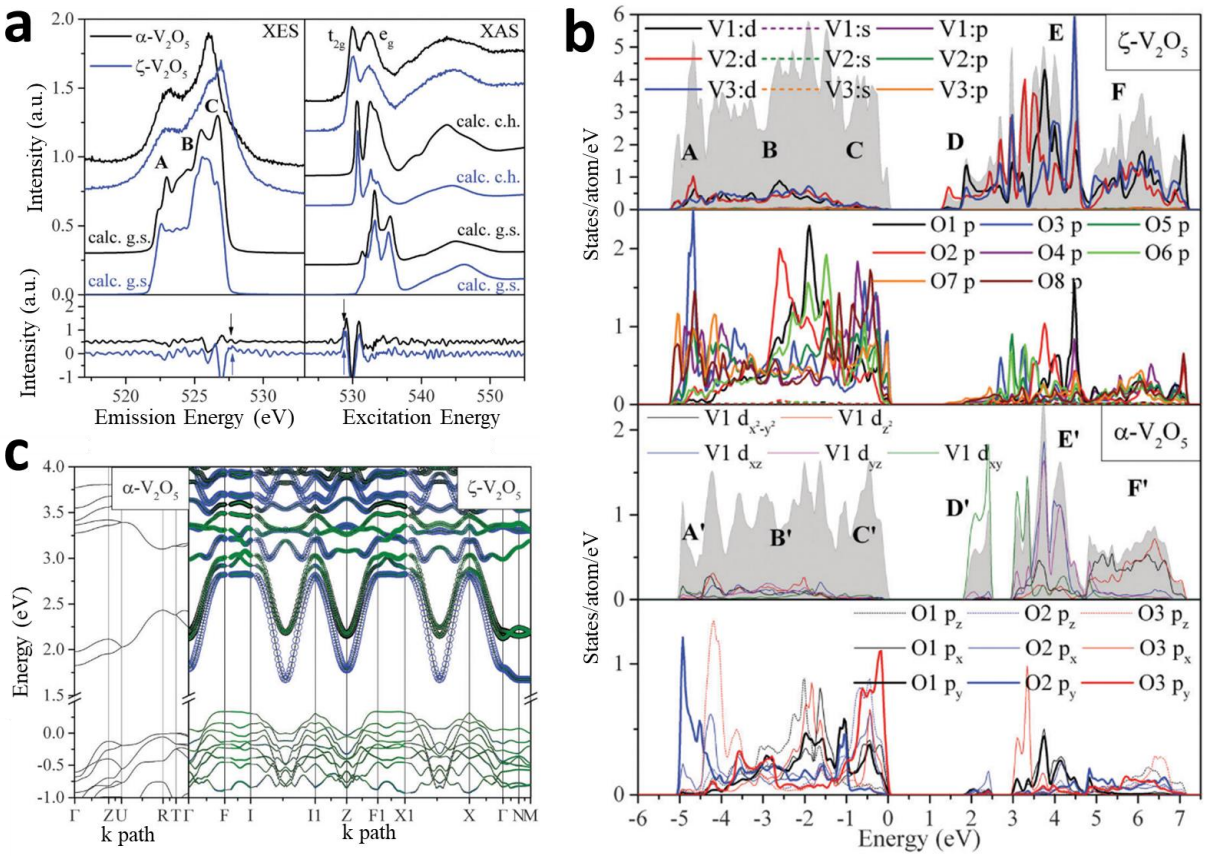

Figure 2.5. (a) XES (left panel) and XAS (right panel) of α- and ζ-V_2O_5 nanowires with t_{2g} and e_g states labelled. (b) DOS of ζ-V_2O_5 (top) and α-V_2O_5 (bottom). (c) Band structure of α-V_2O_5 (left) and ζ-V_2O_5 (right). Reprinted with permission from Ref. 15.

The trend of the direct band gap of α- and ζ-V_2O_5 follows that of the reported indirect band gap values. The latter phase has a lower band gap than the thermodynamically stable α-phase. The

ratio in peak height of t_{2g}/e_g of the reported O K-edge XAS measurements shows an increase from α- to ζ-V_2O_5, indicating an increase in π bonding strength (Figure 2.5a).[15,35] The t_{2g} feature corresponds to the π-interactions that occur between vanadium and oxygen atoms, while e_g corresponds to the σ-interactions.[35] The π-interactions increase in ζ-V_2O_5 since there is an increase in local symmetry with the [VO_6] polyhedra. In Figure 2.5b, the t_{2g} states are indicated by the regions labelled D and E for ζ-V_2O_5 (D' and E' for α-V_2O_5) and the e_g states are labelled as F for ζ-V_2O_5 (F' for α-V_2O_5).[15] The dispersion of bands is also visible in the side-by-side comparison of the DOS of α-V_2O_5 and ζ-V_2O_5 (Figure 2.5c), where the latter shows an increase in band dispersion and a decrease in the energy gap between the valence band edge and conduction band edge.[15] Increase in π bonding strength suggests an increase in covalency in ζ-V_2O_5, therefore there should be a reduction in band gap for the metastable phase compared to the stable α-V_2O_5.

The increase dispersion of the t_{2g} states, specifically the V d_{xy} bands, indicates more π-interactions are occurring in ζ-V_2O_5 (Figure 2.5b).[15] With more π-interactions, the increased covalency gives rise to an increase in overlap of orbitals allowing for the valence and conduction band to be closer together. In addition, greater covalency is known to improve ion transportation for applications such as energy storage.[15,26] Previously reported work by our group shows ζ-V_2O_5 as having more potential as a cathode material than α-V_2O_5 for multivalent rechargeable Mg-batteries owing to the increased covalency. [14] Increased covalency helps to mitigate polaron formation during lithiation by ~50 meV, as well as decrease polaron diffusion barriers more than 100 meV less than α-V_2O_5.[14]

The optical band gaps of these V_2O_5 polymorphs provide useful information to determine the energetic offset of polymorph-V_2O_5/CdSe heterostructures for solar energy conversion.[11] The valence band edge potential of α-V_2O_5 and CdSe QDs were previously determined by hard X-ray

photoemission spectroscopy (HAXPES).[9,11] In addition, as mentioned earlier, the valence band of V_2O_5 polymorphs is dominated by bonding and nonbonding O s- and p-states.[11,15] The energy of O 2p lone-pair states does not vary much with the differences in structure from one polymorph to the next, therefore the valence band edge potential for each polymorph is assumed to be constant.[15] Aligning the valence band edge of α-, γ'-, and ζ-V_2O_5 to the previously reported value, the conduction band edge of each polymorph can be determined by adding the calculated E_g value to the valence band edge.[11] The relative band structure of polymorph-V_2O_5 with respect to CdSe is shown in Figure 2.6.[11] The staggered band gaps between each polymorph of V_2O_5 to CdSe indicates a type II heterojunction between the semiconductors, which can be useful in increasing the electron-hole charge separation for solar energy conversion and photocatalysis.[11]

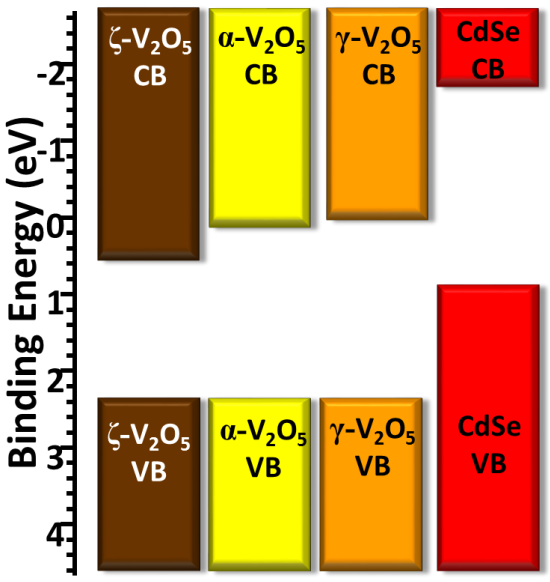

Figure 2.6. The relative band alignment of polymorph V_2O_5/CdSe QDs. Reprinted with permission from Ref. 11. Manuscript in preparation.

When the heterostructure is photoexcited through either the V_2O_5 nanowire or CdSe QDs, the electron-hole pair is generated and separated to different spatial locations across the interface based on the specific offsets across the type II heterojunction.[11] As holes "float up" in energy and electrons "drop down" in energy, the electron-hole pair will be separated regardless of which side of the heterostructure was photoexcited. Based on Figure 2.6, if a polymorph of V_2O_5 was photoexcited, the hole will transfer to the valence band of CdSe whereas the electron will stay in the conduction band of the polymorph. If the CdSe happened to be photoexcited, the hole will remain in the QD's valence band, while the electron will fall to the lower energy conduction bands of the polymorph. Both scenarios lead to the separation of the electron-hole pair across the heterojunction, thus extending the lifetime of the photogenerated electrons and holes by inhibiting direct recombination. Transient absorbance (TA) spectroscopy determined that the average lifetime of the charge separation in the polymorph V_2O_5/CdSe heterostructures increased at least two-fold and some also showed an increase up to one order of magnitude greater when compared to the respective unmodified polymorph V_2O_5, which is ascribed to the successful extraction of photogenerated holes by the semiconductor QDs.[11]

CHAPTER III

ALTERING *x* IN $Cu_xV_2O_5$ BRONZES TO MODIFY THE OPTICAL BAND GAP

3.1 Introduction

Of the numerous polymorphs of V_2O_5, the open-frameworks and accessible sites for cation occupancy lead to a rich group of mixed metal-vanadium oxide bronzes, $M_xV_2O_5$, where M is the intercalated metal-cations (Li^+, Na^+, Mg^{2+}, Cu^+, Ag^+, etc.) and *x* is the metal-cation content.[9,10,16,20–23] The possible variations of M and *x* provide a diverse palette of compounds for exploration into the correlation between the geometric and electronic structure that each bronze may exhibit when each variable is manipulated and tuned. Due to the many possibilities, these bronzes may exhibit interesting properties such as metal-insulator transition (MIT), charge ordering, superconductivity, and paramagnetism.[25]

One of the many vanadium bronzes, $Cu_xV_2O_5$, exist in two different V_2O_5 frameworks: the β/β'-phase with a tunnel-like structure similar to ζ-V_2O_5 and the ε-phase with a double-layered structure (Figure 3.1).[16,20,21,36] The Cu cations in the β'-phase sit in the β'-sites whereas seen earlier, the Ag cations in β-$Ag_xV_2O_5$ reside in larger β-sites. As the sites in which Cu^+ could reside in is restricted to the β'-sites, the stoichiometry of Cu to V_2O_5 is ~0.5 when full. The differences between the two β/β'-sites were depicted in Figure 1.6. Due to the tunnel-like and sheet-like structures of β'- and ε-$Cu_xV_2O_5$, respectively, ion transport is anisotropically confined along the sites available for Cu^+ intercalation.[20] The complete ionization of Cu^+ and the partial cupration of the available intercalation sites in each structure generates charge-ordered patterns of V^{4+} and V^{5+} cations along the frameworks resulting in stabilization of distinct charge-ordering patterns dependent on stoichiometry.[20]

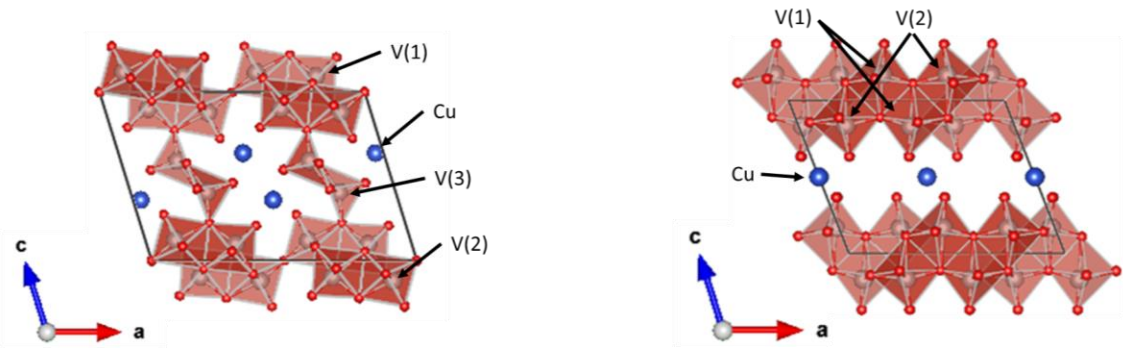

Figure 3.1. Crystal structure of (left) β'-$Cu_{0.5}V_2O_5$ and (right) ε-CuV_2O_5, where the atoms Cu, V, and O atoms are colored blue, gray, and red, respectively.

These correlated $M_xV_2O_5$ bronze systems allow for increased tunabilty of properties such as MIT, superconductivity, etc. *via* synthetic alterations of either the metal-cation identity or its stoichiometry. As previously reported, temperature-driven metal-insulator transitions for β'-$Cu_xV_2O_5$ from a range of 150-395 K as a function of *x*.[20,35] This phenomenon arises from the effective vanadium valence and the extent of electron localization, which is altered with changes in the Cu cation content and ordering within the structure. The changes in local site symmetry and formal valence of vanadium atoms, as seen in the changes of peak positions and relative intensities in the X-ray absorption near-edge structure (XANES) spectra are indicative of changes in electron densities and electronic structure.[35] The DOS of β'-$Cu_xV_2O_5$ with various *x* stoichiometry show the energy band gap increases with each reduction of *x*, as seen in the DFT calculations in Figure 3.2.[37] The Cu 3d mid-gap states occupy the upper part of the valence band and diminish as Cu-content decreases.[37] The synthesis of these two $Cu_xV_2O_5$ bronzes leads to Cu^+-content of 0.5 and 1 for the β'-phase and the ε-phase, respectively.[16,21,36] The amount of Cu^+ in both β'- and ε-$Cu_xV_2O_5$ can be tuned by taking advantage of the Elbs persulfate oxidation reaction with $Na_2S_2O_8$.[16,21,38]

Provided with the ability to manipulate *x*, the bonding motifs of each variation of Cu cation content in the bronze change with the electronic structure.

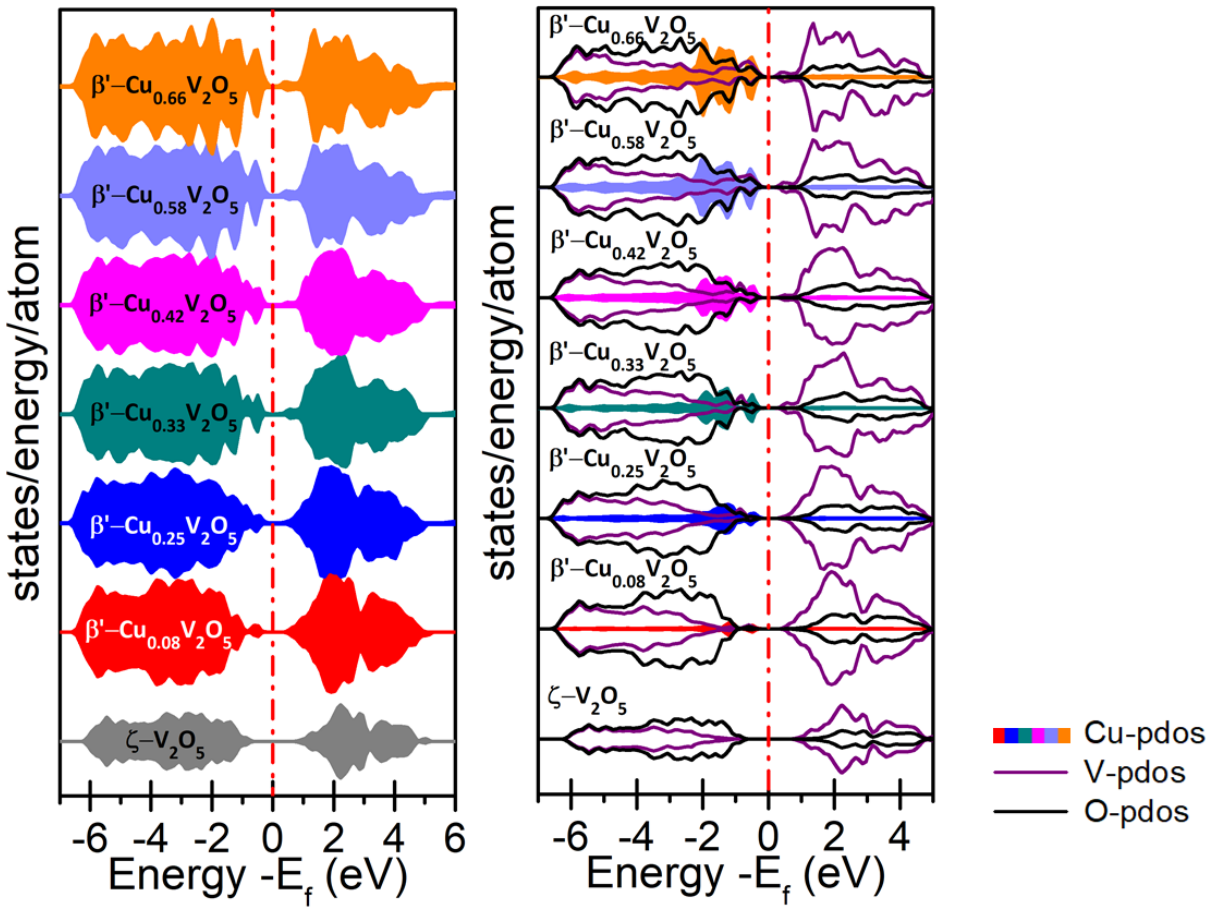

Figure 3.2. (Left) DOS and (Right) projected DOS of β'-$Cu_xV_2O_5$ with various *x* stoichiometries calculated by DFT. Reprinted with permission from Ref. 37. Manuscript in preparation.

In addition, through cation extraction of Cu from β'-$Cu_{0.5}V_2O_5$, the stoichiometry of Cu^+ can be reduced to approximately zero, yielding metastable ζ-V_2O_5 polymorph.[21] Although a mechanism to synthesize ζ-V_2O_5 was expanded on earlier, the method leaves a substantial remnant amount of Ag within the tunnels (estimated to be x ~0.04). When the intercalated Ag ions are

removed from the precursor, β-$Ag_{0.33}V_2O_5$, *via* acidic conditions, a considerable amount of Ag^+ remains within the structure producing something closer to β-$Ag_{0.04}V_2O_5$ rather than the completely empty tunnel-like structure of ζ-V_2O_5.[10,21] The β'-$Cu_xV_2O_5$ family provides a method to obtain a de-intercalated sample of ζ-V_2O_5, as well as a way to study electron-correlation while altering metal cation content.

3.2 Synthesis and Characterization of Two-Phases of $Cu_xV_2O_5$

3.2.1 Synthesis of β'- and ε-$Cu_xV_2O_5$ Bronzes

The synthesis of β'-$Cu_{0.5}V_2O_5$, as developed by our group, utilized hydrothermal conditions in a 125 mL capacity Teflon-lined stainless-steel autoclave.[21] In a stoichiometric ratio of 2:1:1 of $VO(C_5H_7O_2)_2$ (~0.90 g), $Cu(NO_3)_2{\cdot}2.5H_2O$ (~0.39 g), and V_2O_5 (~ 0.31 g) were added to 86 mL of deionized water in the autoclave. The sealed autoclave was placed in a 210°C oven for 24 hours. After 24 hours, the autoclave was removed and brought to room temperature. The resulting product was filtered and washed with copious amounts of water and 2-propanol. The material was allowed to dry in air overnight, resulting in β'-$Cu_{0.5}V_2O_5$ as per:

$$2VO(C_5H_7O_2)_2\ (aq.) + Cu(NO_3)_2\ (aq.) + V_2O_5\ (s) + 3H_2O\ (l) \rightarrow$$
$$2\beta'\text{-}Cu_{0.5}V_2O_5\ (s) + 4C_5H_8O_2\ (l) + 2HNO_3\ (aq.) \quad (6)$$

The synthesis of ε-CuV_2O_5 followed similar procedures to that of the β-$Cu_{0.5}V_2O_5$ polymorph with the exception of the exclusion of the V_2O_5 precursor[36]:

$$2VO(C_5H_7O_2)_2\ (aq.) + Cu(NO_3)_2\ (aq.) + 3H_2O\ (l) \rightarrow$$
$$\varepsilon\text{-}CuV_2O_5\ (s) + 4C_5H_8O_2\ (l) + 2HNO_3\ (aq.) \quad (7)$$

The reaction mixture of ~0.21 g $VO(C_5H_7O_2)$ and ~0.09 g $Cu(NO_3)_2{\cdot}2.5H_2O$ was added to 15 mL of water and 1 mL of 2-propanol in a 23 mL capacity Teflon-lined stainless-steel autoclave. The

autoclave was then placed into an oven at 210°C for 24 hours, after which the cooling, washing, and drying procedures of β'-$Cu_{0.5}V_2O_5$ were followed. Both Cu-bronzes were ground into a fine powder using a mortar and pestle for the following procedures.

3.2.2 Removal of Cu from β'- and ε-$Cu_xV_2O_5$ Bronzes

The amount of Cu^+ in each of the two $Cu_xV_2O_5$ bronzes can be tuned with further synthetic approaches. After obtaining the products dried and in powder form after being ground with a mortar and pestle, the amount of Cu^+ was manipulated using aqueous $Na_2S_2O_8$, following the Elbs persulfate oxidation reaction.[16,21,38] Stoichiometric amounts of $Na_2S_2O_8$ to Cu^+-content (0.35 – 10, $Na_2S_2O_8$:Cu^+) were combined in 20 mL of deionized water and stirred for 24 h at 70°C under ambient atmosphere to leach amounts of Cu from each structure.[21] To remove Cu^+ from β'-$Cu_{0.5}V_2O_5$ entirely in order to obtain ζ-V_2O_5, 1:1 Cu^+ to $Na_2S_2O_8$ were added in a similar manner:

$$2\beta'\text{-}Cu_{0.5}V_2O_5\ (s) + Na_2S_2O_8\ (aq.) \xrightarrow{70°C} 2\zeta\text{-}V_2O_5\ (s) + Na_2SO_4\ (aq.) + CuSO_4\ (aq.) \quad (8)$$

Obtaining ε'-V_2O_5 from ε-$Cu_{0.5}V_2O_5$ followed the same 1:1 Cu^+ to $Na_2S_2O_8$ reaction ratio as seen below:

$$\varepsilon\text{-}CuV_2O_5\ (s) + Na_2S_2O_8\ (aq.) \xrightarrow{70°C} \varepsilon'\text{-}V_2O_5\ (s) + Na_2SO_4\ (aq.) + CuSO_4\ (aq.) \quad (9)$$

To vary the amount of Cu^+ leftover in the V_2O_5 framework, the ratio of Cu^+ to $Na_2S_2O_8$ was varied. The resulting materials were washed with deionized water to remove side products, such as Na_2SO_4 and $CuSO_4$. The dried materials showcased a variety of colors with each additional addition of $Na_2S_2O_8$, indicating an obvious change in optical E_g.

3.2.3 Characterization

Powder X-ray diffraction data were acquired on a Bruker D8 Focus-Eco diffractometer (Cu Kα, λ = 1.5418 Å source). Diffuse reflectance data were collected from 200 – 800 nm on a Hitachi

U-4100 UV-vis-NIR spectrophotometer with the Praying Mantis™ attachment for powder samples. In addition, Cu to V content was determined using PerkinElmer NexION 300D inductively-coupled plasma mass spectrometry (ICP-MS), where ~5-10 mg of each sample was added into separate 50 mL centrifuge tubes containing 1 mL of concentrated HNO_3 each. The solution was allowed to sit at room temperature for ~20 minutes before 1 mL of concentrated HCl was added. The tubes were then centrifuged to mix the solution. Afterwards, the solutions were heated to 75ºC until the solutions were clear. The solutions were allowed to cool down to room temperature, after which, water was added to each tube until the total volume read 50 mL. Using 1% (v/v) HNO_3 and water as the reagent blank, 1000-fold dilutions (50 µL to 50 mL) were prepared of each solution with the blank for the ICP-MS analysis.

3.3 Results and Discussion

After decupration of the initial precursor β'-$Cu_{0.5}V_2O_5$ by varying the amount of $Na_2S_2O_8$ added, a gradual color change from dark green to dark yellow and dark brown occurred as shown on the right-hand side of Figure 3.3. Subtle changes in the XRD reflections occur as well. Through ICP-MS, it's determined that the precursor initially started with x~0.48. When the molecular percent of $Na_2S_2O_8$ to Cu-content (x~0.5) of the precursor was varied from 0.35, 0.5, 0.75, 3, and 10, the final β'-$Cu_xV_2O_5$ products yielded x~0.27, 0.093, 0.0695, 0.0519, and 0.0179, respectively, as determined from the mass fractions obtained from ICP-MS results. As shown with the last sample, the leftover Cu cation content is very close to zero, therefore it can be considered ζ-V_2O_5. The amount of Cu^+ left in the ζ-V_2O_5 from this method, x ~ 0.0179, is less than the amount of Ag^+ left in ζ-V_2O_5 when using the silver deintercalation method with β-$Ag_{0.33}V_2O_5$ precursor. This decupration method allows for a better control of x, as well as a more efficient synthetic pathway

to obtaining ζ-V_2O_5 with close to no intercalated Cu-cations left within the framework. This verifies work done by Andrews *et al*, where obtaining an empty tunnel-like open framework structure of ζ-V_2O_5 has shown potential as a cathode material for multivalent, rechargeable Mg-batteries.[14,21]

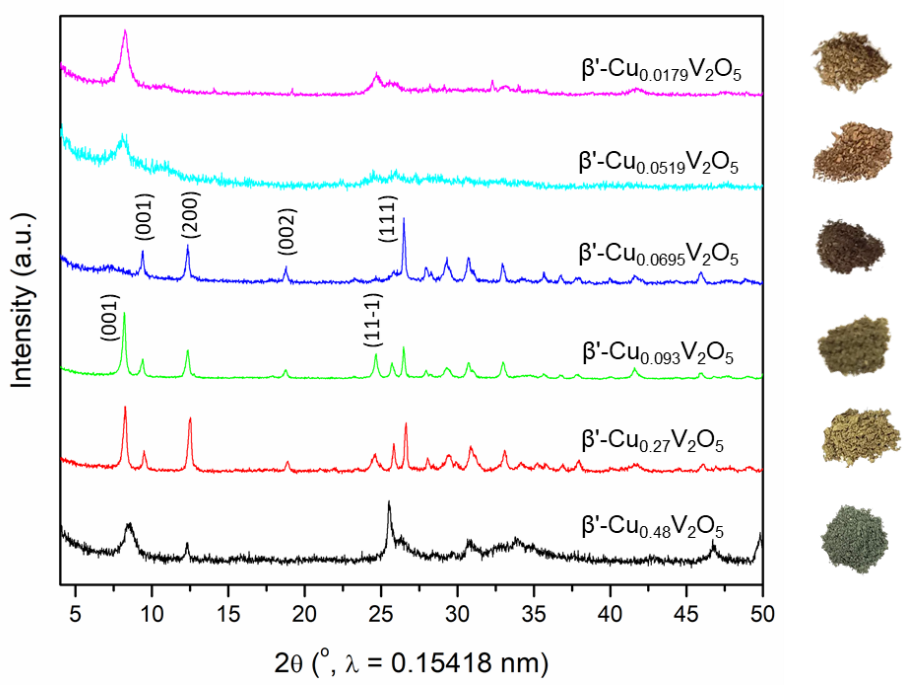

Figure 3.3. XRD patterns of β'-$Cu_xV_2O_5$ with varying Cu cation content. The corresponding colors of each material measured are to the right of the pattern.

Due to the changes in color as seen above, it is expected that the optical band gap varies from one sample to the next since color corresponds to the wavelength and energy of light that is absorbed. Band gaps were determined in a similar fashion as with the V_2O_5 polymorphs. The E_g trend by Cu-content can be seen in Figure 3.4. Tabulated in the inset of Figure 3.4, the band gap starts at 2.52 eV for the firstly synthesized β'-$Cu_{0.48}V_2O_5$, which is the highest measured value

amongst this set of bronzes. The band gap slowly decreases until a certain Cu^{+} content is reached and then becomes essentially constant, presented in the inset of Figure 3.4.

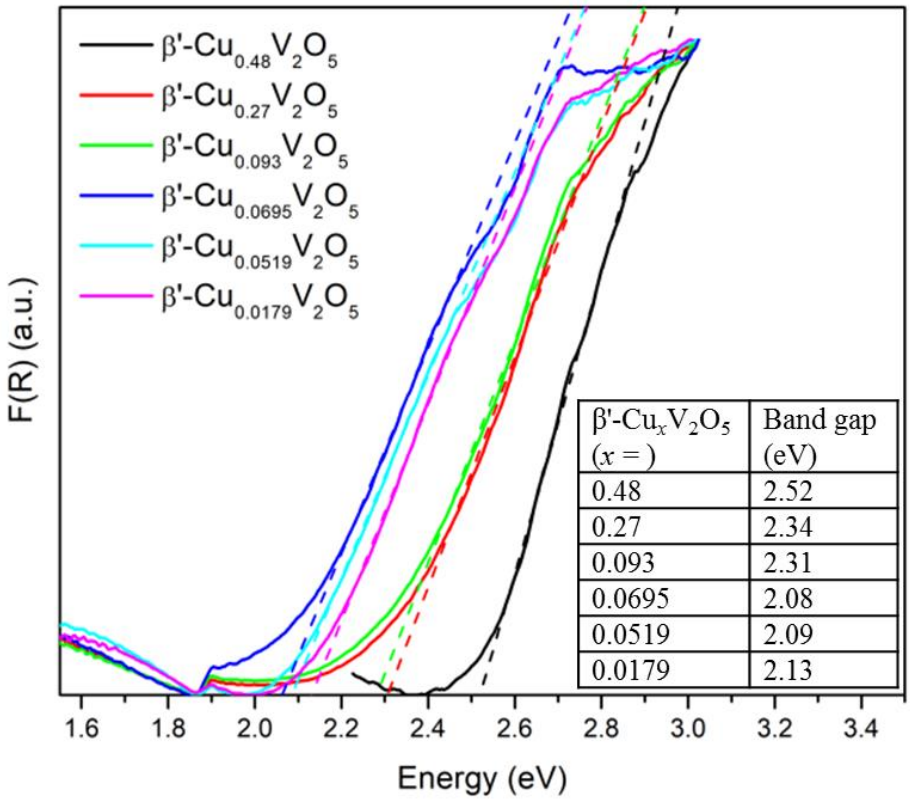

β'-$Cu_xV_2O_5$ (x =)	Band gap (eV)
0.48	2.52
0.27	2.34
0.093	2.31
0.0695	2.08
0.0519	2.09
0.0179	2.13

Figure 3.4. Diffuse reflectance paired with Kubelka-Munk analysis for β'-$Cu_xV_2O_5$ with various amounts of Cu. The inset shows the E_g of each bronze deduced from this method *x*.

As mentioned in Chapter 2.3, the band gap of ζ-$(Ag_{0.04})V_2O_5$ is 2.09 eV when synthesized through silver deintercalation of β-$Ag_{0.33}V_2O_5$. When the Cu stoichiometry in β'-$Cu_xV_2O_5$ is less than 0.0695, the band gap becomes constant and closely resembles that of ζ-$(Ag_{0.04})V_2O_5$, indicating that the similar amount of metal intercalated affects the atomistic structure of the V_2O_5 framework in both β'-$Cu_{0.0519}V_2O_5$ and ζ-$(Ag_{0.04})V_2O_5$, bringing about a slight lattice expansion.

Because the physical structures are comparable, the electronic structures will exhibit similar features. The β/β'-phases of $M_xV_2O_5$ (*C2/m*) has three distinct vanadium-centered polyhedral: edge-sharing $V(1)O_6$ distorted octahedra, corner-sharing $V(2)O_6$ distorted octahedra, and $V(3)O_5$ square pyramids, much like ζ-V_2O_5.[4,10] The tunnel-like enclosure that forms along the *b*-axis is either empty (ζ-V_2O_5) or filled with metal ions intercalated in either the β- or β'-sites for β/β'-$M_xV_2O_5$, respectively. This open-tunnel framework is preserved when emptied or filled; however, the electronic structure is altered with respect to amount of metal ion intercalated in the tunnels as seen with the changing of E_g depending on x for β'-$Cu_xV_2O_5$.

The trend of the electronic structure and bonding motifs of β'-$Cu_xV_2O_5$ with changing metal ion stoichiometry is expected to be analogous to the β-$Ag_xV_2O_5$ values. Emptying and removing the ions from their respective tunnel-sites causes the number of electrons localized on the vanadium oxide framework to decrease.[10] This slight oxidation of the framework causes a decrease in V^{4+} presence, in favor of V^{5+}. As the average oxidation number of V increases and the V—O bonds become weaker and less covalent. Therefore, the E_g decreases along with decreasing x as smaller E_g corresponds with the less covalent bonding. For this tested set of β'-$Cu_xV_2O_5$, the E_g decreases when the Cu-content is between about $0.48 < x < 0.0519$. The band gap increases slightly from Cu-content of 0.0659 to 0.0519, however the value is within error of one another, therefore $x \approx 0.0519$ is considered to follow this trend. In addition, the final sample, β'-$Cu_{0.0179}V_2O_5$, shows an increase in band gap of ~0.04 eV, but could be considered within error to the band gaps when Cu^+-content is 0.0659 or 0.0519. As the amount of Cu^+ intercalated within the tunnel structure decreases, the E_g eventually becomes constant at around ~2.10 eV.

As for the ε-phase of $Cu_xV_2O_5$, this bronze portrays a double-layered structure formed by layers of connected $[V_4O_{10}]$ polyhedra with Cu cations intercalated between the layers. The

amount of Cu^{+} was tuned in the same manner as with the β'-phase. The diffraction pattern of the precursor ε-CuV_2O_5, seen in Figure 3.5, coincided with the calculated reflections for ε-$Cu_{0.85}V_2O_5$, while the subsequent ε-$Cu_xV_2O_5$ exhibited the (00*l*) reflections similar to those reported for ε'-V_2O_5 due to the anisotropy of the double layers.[16,36,39,40] The reflections of the final sample, ε-$Cu_{0.16}V_2O_5$, are broad and difficult to assign using XRD as the double layers at this point show great expansion, as well as some exfoliation. The color of the samples changes from a dark black powder to green and then to brown are perceived with each extra addition of $Na_2S_2O_8$ to the ε-CuV_2O_5 precursor, as seen on the right-hand side of Figure 3.5.

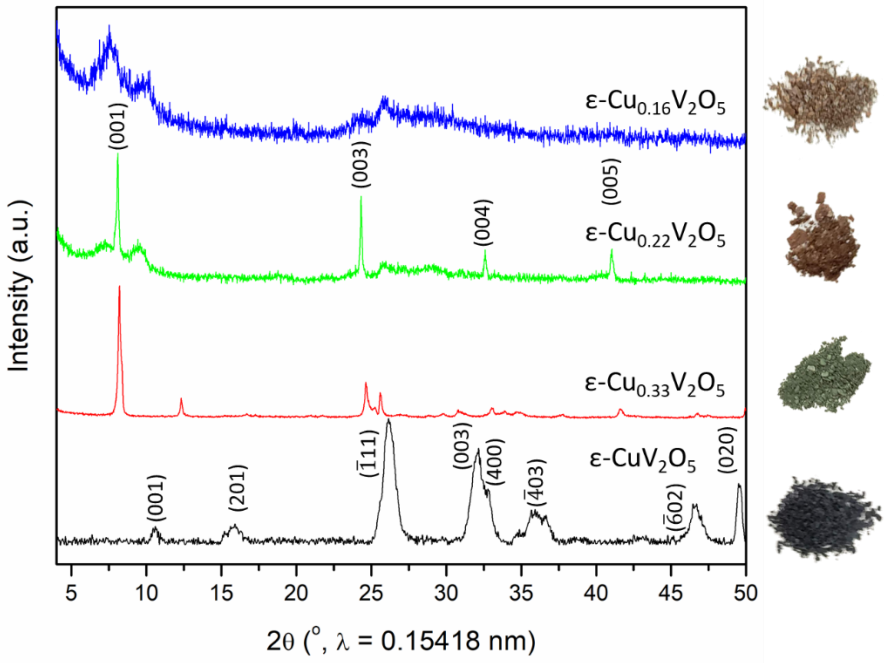

Figure 3.5. XRD patterns and powder images of the ε-$Cu_xV_2O_5$ set. Color changes occur for the as-prepared samples.

The diffuse reflectance spectra of the starting precursor material, ε-CuV_2O_5, did not show any linear features, as indicated in Figure 3.6a. The black color of ε-CuV_2O_5 somewhat provides an indication of the expected reflectance values. As a black color is seen, the material is assumed to absorb at all wavelengths. However, to the human eye, that may not necessarily be appropriate to assume the black material absorbs at all wavelengths and therefore reflects nothing at all wavelengths.[41] The DRS plot of ε-CuV_2O_5 shows an average reflectance of 0.37% from the wavelength range of 250 - 800 nm (Figure 3.6a), indicating that all visible light is absorbed. This reveals ε-CuV_2O_5 as a metallic material with no band gap due to the large amounts of Cu-cations intercalated in the structure. Metallic properties such as high conductivity and energy density have previously been reported as a reason for ε-CuV_2O_5 being a promising cathode material for energy storage.[36]

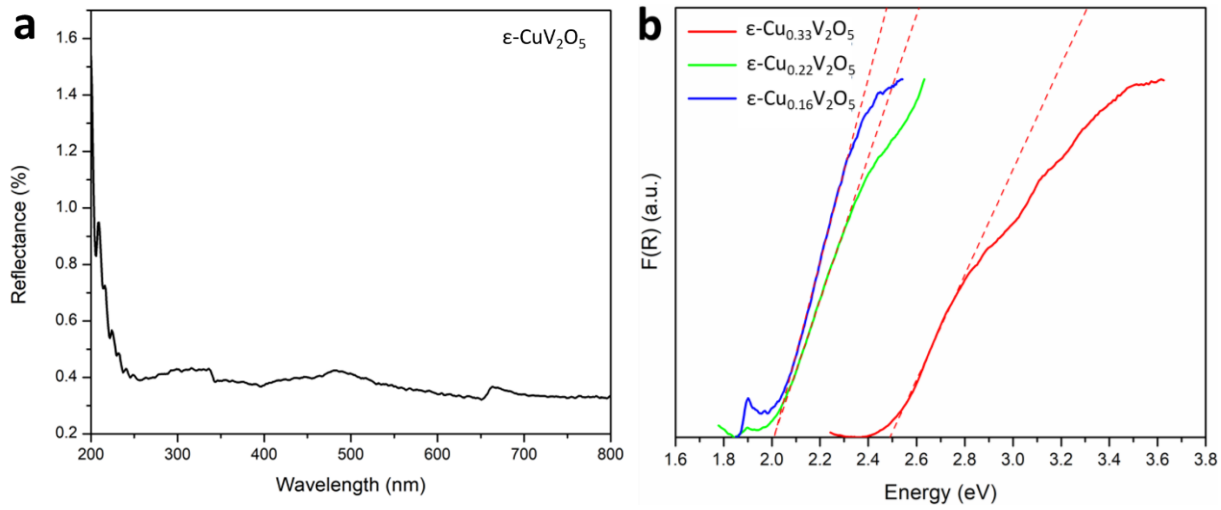

Figure 3.6. (a) Diffuse reflectance spectra of precursor ε-CuV_2O_5. (b) Band gap determination of ε-$Cu_xV_2O_5$.

The E_g determination for the following ε-$Cu_xV_2O_5$ material was more straightforward. The E_g for ε-$Cu_xV_2O_5$ with x~0.33, 0.22, and 0.16 is 2.49, 2.01, and 2.01 eV, respectively. From ε-CuV_2O_5 to ε-$Cu_{0.33}V_2O_5$, there is a large increase in E_g as the material is no longer metallic. When the Cu cations are removed, water molecules are introduced into the interstitial sites between the layers of the V_2O_5 framework. The confinement of water causes the interlayer separation to increase as indicated by the shift of the (001) reflection to lower 2θ values in Figure 3.5 when Cu-content is less than $x \sim 1$. These trends lead to an increase in E_g as the electron density of the V_2O_5 framework become more separated. The position of the (001) reflections for x~0.33, 0.22, and 0.16 does not vary much, therefore the effect of the water-mediated interlayer separation may not play a large role in the changes that occur with the E_g among these three samples.

The E_g decreases from 2.49 eV to 2.01 eV, where the latter value remains constant for Cu-content of 0.22 and 0.16. With less intercalated Cu cations present, the V—O bonding strength increases as the interactions between the Cu cations and the V_2O_5 framework decreases and become less polarizable.[16] As will be mentioned in more detail later, the E_g determined *via* DRS with Kubelka-Munk theory is for the entire material. The decrease in E_g when x~0.22 and 0.16 indicates a more covalent structure in contrast to when x~0.33. The electron density increases around the V-sites as V—O bonding strengthens, while the intercalated Cu cations interact more covalently with the framework. Overall, the structure shows increase in covalent nature as indicated by the decrease in E_g.

The experimental E_g determined by a combination of XAS and DFT calculations for ε'-V_2O_5 was reported to be 3.27 ± 0.20 eV.[16] This may seem counterintuitive to the dark brown colors seen for ε-$Cu_{0.16}V_2O_5$ in Figure 3.5, as darker colors indicate relatively smaller E_g than materials with lighter colors. However, as explained by Tolhurst, *et al.*, the reported E_g is specific for the

VO layers only, reflecting the indirect bandgap, disregarding the possible interstitial water molecules that may have remained between the double-layers during the decupration procedures.[16] DRS with Kubelka-Munk theory does not discriminate between the VO layers and the remnant water molecules. This leads to the determined E_g of 2.01 eV, which is more reflective of the visible brown color of ε-$Cu_{0.16}V_2O_5$. In addition, this sample contains ~0.16 Cu to V_2O_5, causing more difficulties when comparing to the reported data of a more pure sample without much Cu cation content, ε'-V_2O_5.

The small E_g of ε-$Cu_{0.16}V_2O_5$ indicates the covalency of the material. As mentioned earlier, materials with more covalent nature make for better cathode materials for batteries.[14,16] Covalency allows for improved diffusion kinetics and reduced transport barriers due to the reduction of the polaron mass in the materials, where the polaron represents electrons that localize on the V_2O_5 framework as a result of coupling with local structural distortions.[16,18] Polymorph ζ-V_2O_5 has a E_g of 2.09 eV, whereas the E_g of ε-$Cu_{0.16}V_2O_5$ is 2.01 eV indicating greater potential for the latter to exceed as a cathode material. Lithium-ion batteries using ε-$Cu_{0.95}V_2O_5$ provided high electroactivity and remarkable reversibility with both Cu and V being redox active.[36] This verifies the potential of ε-$Cu_{0.16}V_2O_5$ for energy storage, however, as mentioned above, water is present in the galleries, which has the potential to deleteriously affect the electrochemical behavior. Full dehydration of these materials is necessary in order to explore such properties.

CHAPTER IV

OUTLOOKS: SUMMARY AND CHALLENGES

4.1 Summary

Vanadium oxide, V_2O_5, exists in the form of different polymorphs with vastly different atomic structures, bonding motifs, and V—O connectivity. The atomistic structure and connectivity profoundly alter the electronic structure of the polymorphs yielding a diverse range of compounds with varying band gaps. In addition to binary V_2O_5, the open framework structure of these polymorphs can incorporate metal cations to form mixed-metal oxides of different phases, $M_xV_2O_5$. The intercalating cation and its content in each $M_xV_2O_5$ bronze can be tuned across specific compositional ranges allowing for considerable tunability of the bandgap. The underlying physical and electronic structures dictate the possible applications of these materials in charge storage, charge transfer, catalysis, etc.

An important measurement of the electronic structure is the band gap, E_g. One method to elucidate the E_g of these different polymorphs involves the use of diffuse reflectance spectroscopy along with Kubelka-Munk theory. This method provides a facile route to determine E_g of powdered materials without interference from substrate effects. The determined band gap values provide insight into the energetic offsets of V_2O_5/QD heterostructures constituted from different polymorphs. The measurements further allow for an evaluation of the influence of metal cation content on the electronic structure of $M_xV_2O_5$ bronzes. The E_g of several polymorphs of V_2O_5, along with two different phases of $Cu_xV_2O_5$ bronzes with varying Cu^+ stoichiometry, was determined. The band gaps of bulk, α-, γ'-, and ζ-V_2O_5 are 2.29, 2.31, 2.36, and 2.09 eV, respectively. As for β'-$Cu_xV_2O_5$, the band gap decreases from 2.25 to 2.09 eV when x decreases from 0.48 to 0.0519. Afterwards, the band gap becomes constant with decreasing x. The ε-phase

of $Cu_xV_2O_5$ provided a metallic material as ε-CuV_2O_5 did not show any features in the diffuse reflectance spectra. Varying the Cu-cation content of ε-$Cu_xV_2O_5$ to 0.33, 0.22, and 0.16, the band gaps were determined as 2.49, 2.01, and 2.01 eV, respectively.

The determination of E_g of V_2O_5 polymorphs and $M_xV_2O_5$ bronzes does not necessarily stop at these sample sets. The δ'-phase of V_2O_5 has been reported, however the E_g was not determined here.[19] DRS with Kubelka-Munk could be applied to the double-layered δ'-V_2O_5 and a comparison with another double-layered polymorph, ε'-V_2O_5, may provide insight into how the small structural differences, in the form of layer shifting, can affect the electronic structure. In addition, as mentioned earlier, there is an abundance of $M_xV_2O_5$ bronzes, where M is the metal cation intercalated in the V_2O_5 framework. The identity of "M" covers alkali and alkaline metals, transition metals, post-transition-metal main group cations, and even organic cations.[19] Many of the variations of these mixed metal oxides have the potential to be fully or partially deintercalated, allowing for some control on the stoichiometry and tunabilty of the electronic structure, which could be explored using the techniques mentioned in the work.

The electronic structure and density of states determination by DFT of these different polymorphs and bronzes can also benefit from the E_g calculated by DRS with Kubelka-Munk theory. As mentioned earlier, DFT predictions are limited by assumptions made about electron—electron interactions. DFT calculations could be enhanced to more accurately predict the corresponding electronic structure where the separation of states more closely follows the known band gap.

As mentioned, ζ-V_2O_5 has more potential as a cathode material than α-V_2O_5 due to its more covalent nature indicated by the smaller E_g. A possible application of ζ-V_2O_5 can be in multivalent Ca-ion batteries for energy storage. As a new battery technology, Ca-ion battery development faces

roadblocks in the form of possible electrolytes and possible cathode materials that could work in this system. Recently, a nonaqueous electrolyte ($Ca(PF_6)_2$) was shown to reversibly intercalate Ca-cations in a battery.[3] A potential cathode for this electrolyte for Ca-ion battery could be ζ-V_2O_5, which already showed better potential for Mg-ion batteries than α-V_2O_5.

4.2 Challenges

A challenge that diffuse reflectance spectroscopy faces is the lack of selectivity. In the event of water impurities that may occur when using aqueous $Na_2S_2O_8$ for Cu-deintercalation from the two $Cu_xV_2O_5$ bronzes, the determined E_g will be affected. The method used in this work will determine the overall E_g rather than just focus on the V_2O_5 framework as XAS could. Greater focus on dehydration of the resulting Cu-bronzes or formulation of a water-less synthesis will allow for a more accurately measured E_g by DRS. Due to the potential of ε'-V_2O_5 as a cathode material for energy storage in the form of batteries, the removal of all interstitial water is necessary, regardless of the method used to determine E_g.

In addition, this method elucidates allowed electron transitions while neglecting forbidden indirect transitions, which are of importance to luminescent materials. Optical luminescence depends strongly on the site and chemical environment of the absorbing atom.[42] Being able to probe forbidden transitions would provide a better understand structural and electronic properties of luminescent materials.

REFERENCES

(1) De Jesus, L. R.; Andrews, J. L.; Parija, A.; Banerjee, S. Defining Diffusion Pathways in Intercalation Cathode Materials: Some Lessons from V_2O_5 on Directing Cation Traffic. *ACS Energy Lett.* **2018**, *3*, 915–931.

(2) Tarascon, J.-M.; Armand, M. Issues and Challenges Facing Rechargeable Lithium Batteries. *Nature* **2001**, *414*, 359–367.

(3) Lipson, A. L.; Pan, B.; Lapidus, S. H.; Liao, C.; Vaughey, J. T.; Ingram, B. J. Rechargeable Ca-Ion Batteries: A New Energy Storage System. *Chem. Mater.* **2015**, *27*, 8442–8447.

(4) Parija, A.; Liang, Y.; Andrews, J. L.; De Jesus, L. R.; Prendergast, D.; Banerjee, S. Topochemically De-Intercalated Phases of V_2O_5 as Cathode Materials for Multivalent Intercalation Batteries: A First-Principles Evaluation. *Chem. Mater.* **2016**, *28*, 5611–5620.

(5) Kim, H.; Jeong, G.; Kim, Y.-U.; Kim, J.-H.; Park, C.-M.; Sohn, H.-J. Metallic Anodes for next Generation Secondary Batteries. *Chem. Soc. Rev.* **2013**, *42*, 9011–9034.

(6) Bhatt, M. D.; O'Dwyer, C. Recent Progress in Theoretical and Computational Investigations of Li-Ion Battery Materials and Electrolytes. *Phys. Chem. Chem. Phys* **2015**, *17*, 4799–4844.

(7) Yoo, H. D.; Shterenberg, I.; Gofer, Y.; Gershinsky, G.; Pour, N.; Aurbach, D. Mg Rechargeable Batteries: An on-Going Challenge. *Energy Environ. Sci.* **2013**, *6*, 2265–2279.

(8) Parija, A.; Prendergast, D.; Banerjee, S. Evaluation of Multivalent Cation Insertion in Single-and Double- Layered Polymorphs of V_2O_5. *ACS Appl. Mater. Interfaces* **2017**, *9*, 23756–23765.

(9) Pelcher, K. E.; Milleville, C. C.; Wangoh, L.; Chauhan, S.; Crawley, M. R.; Marley, P. M.; Piper, L. F. J.; Watson, D. F.; Banerjee, S. Integrating β-$Pb_{0.33}V_2O_5$ Nanowires with CdSe Quantum Dots: Toward Nanoscale Heterostructures with Tunable Interfacial Energetic Offsets for Charge Transfer. *Chem. Mater.* **2015**, *27*, 2468–2479.

(10) Marley, P. M.; Abtew, T. A.; Farley, K. E.; Horrocks, G. A.; Dennis, R. V; Zhang, P.; Banerjee, S. Emptying and Filling a Tunnel Bronze. *Chem. Sci.* **2015**, *6*, 1712.

(11) Cho, J.; Sheng, A.; Ly, C.; Andrews, J. L.; Sfeir, M. Y.; Watson, D. F.; Banerjee, S. *Efficient Charge Transfer within Type II Interfacial Energetic Offset Using Polymorph V_2O_5/CdSe Heterostructure Platforms with Tunable Energy Band Alignment to Create Long-Lived Charge Carriers*; **2018**. Manuscript in preparation.

(12) Brus, L. Electronic Wave Functions In Semiconductor Clusters: Experiment and Theory. *J. Phys. Chem* **1986**, *90*, 2555–2560.

(13) Cho, J.; Choi, Y.-H.; O'Loughlin, T. E.; De Jesus, L.; Banerjee, S. Ligand-Mediated Modulation of Layer Thicknesses of Perovskite Methylammonium Lead Bromide Nanoplatelets. *Chem. Mater.* **2016**, *28*, 6909–6916.

(14) Andrews, J. L.; Mukherjee, A.; Yoo, H. D.; Parija, A.; Marley, P. M.; Fakra, S.; Prendergast, D.; Cabana, J.; Klie, R. F.; Banerjee, S. Reversible Mg-Ion Insertion in a Metastable One-Dimensional Polymorph of V_2O_5. *Chem* **2018**, *4*, 564–585.

(15) Tolhurst, T. M.; Leedahl, B.; Andrews, J. L.; Marley, P. M.; Banerjee, S.; Moewes, A. Contrasting 1D Tunnel-Structured and 2D Layered Polymorphs of V_2O_5: Relating Crystal Structure and Bonding to Band Gaps and Electronic Structure. *Phys. Chem. Chem. Phys.* **2016**, *18*, 15798–15806.

(16) Tolhurst, T. M.; Leedahl, B.; Andrews, J. L.; Banerjee, S.; Moewes, A. The Electronic Structure of ε'-V_2O_5: An Expanded Band Gap in a Double-Layered Polymorph with Increased Interlayer Separation. *J. Mater. Chem. A* **2017**, *5*, 23694.

(17) Horrocks, G. A.; Likely, M. F.; Velazquez, J. M.; Banerjee, S. Finite Size Effects on the Structural Progression Induced by Lithiation of V_2O_5: A Combined Diffraction and Raman Spectroscopy Study. *J. Mater. Chem. A* **2013**, *1*, 15265.

(18) Horrocks, G. A.; Parija, A.; De Jesus, L. R.; Wangoh, L.; Sallis, S.; Luo, Y.; Andrews, J. L.; Jude, J.; Jaye, C.; Fischer, D. A.; Prendergast, D.; Piper, L. F. J.; Banerjee, S. Mitigating Cation Diffusion Limitations and Intercalation-Induced Framework Transitions in a 1D Tunnel-Structured Polymorph of V_2O_5. *Chem. Mater.* **2017**, *29*, 10386–10397.

(19) Parija, A.; Waetzig, G. R.; Andrews, J. L.; Banerjee, S. Traversing Energy Landscapes Away from Equilibrium: Strategies for Accessing and Utilizing Metastable Phase Space. *J. Phys. Chem. C* **2018**.

(20) Marley, P. M.; Horrocks, G. A.; Pelcher, K. E.; Banerjee, S. Transformers: The Changing Phases of Low-Dimensional Vanadium Oxide Bronzes. *Chem. Commun.* **2015**, *51*, 5181–5198.

(21) Andrews, J. L.; Gross, M. A.; Banerjee, S. *Scalable Topochemical Approach to Charge-Ordered and Metastable Tunnel-Structured V_2O_5*; **2018**. Manuscript in preparation.

(22) Safrany Renard, M.; Emery, N.; Baddour-Hadjean, R.; Pereira-Ramos, J.-P. γ'-V_2O_5: A New High Voltage Cathode Material for Sodium-Ion Battery Na Insertion Na-Ion Battery High Voltage Cathode Vanadium Pentoxide. *Electrochem. Acta* **2017**, 252, 4–11.

(23) Marley, P. M.; Singh, S.; Abtew, T. A.; Jaye, C.; Fischer, D. A.; Zhang, P.; Sambandamurthy, G.; Banerjee, S. Electronic Phase Transitions of δ-$Ag_xV_2O_5$ Nanowires: Interplay between Geometric and Electronic Structures. *J. Phys. Chem. C* **2014**, *118*, 21235–21243.

(24) Yamada, H.; Ueda, Y. Structural and Electric Properties of β'-$Cu_xV_2O_5$. *J. Phys. Soc. Japan* **2000**, *69*, 1437–1442.

(25) Wu, T.-L.; Stabile, A. A.; Patridge, C. J.; Banerjee, S.; Sambandamurthy, G. Electrically Driven Metal-Insulator Switching in δ−$K_xV_2O_5$ Nanowires. *Appl. Phys. Lett.* **2012**, *101*, 163502.

(26) C. Kittel. *Introduction to Solid State Physics*, 8th ed.; Wiley: New York, 2005.

(27) Sangiorgi, N.; Aversa, L.; Tatti, R.; Verucchi, R.; Sanson, A. Spectrophotometric Method for Optical Band Gap and Electronic Transitions Determination of Semiconductor Materials. *Opt. Mater. (Amst).* **2017**, *64*, 18–25.

(28) Eyert, V.; Höck, K.-H. Electronic Structure of V_2O_5: Role of Octahedral Deformations. *Phys. Rev. B* **1998**, *57*, 12727–12737.

(29) Perdew, J. P. Density Functional Theory and the Band Gap Problem. *Int. J. Quantum Chem. Quantum Chem. Symp.* **1986**, *19*, 497–523.

(30) Escobedo Morales, A.; Sánchez Mora, E.; Pal, U. Use of Diffuse Reflectance Spectroscopy for Optical Characterization of Un-Supported Nanostructures. *Rev. Mex. Física S* **2007**, *53*, 18–22.

(31) Bredas, J.-L. Mind the Gap! *Mater. Horizons* **2014**, *1*, 17–19.

(32) Lopez, R.; Gomez, R. Band-Gap Energy Estimation from Diffuse Reflectance Measurements on Sol-Gel and Commercial TiO_2: A Comparative Study. *J. Sol-Gel Sci. Technol.* **2012**, *61*, 1–7.

(33) Cocciantelli, J. M.; Gravereau, P.; Doumerc, J. P.; Pouchard, M.; Hagenmuller, P. On the Preparation and Characterization of a New Polymorph of V_2O_5. *J. Solid State Chem.* **1991**, *93*, 497–502.

(34) Galy, J. Vanadium Pentoxide and Vanadium Oxide Bronzes-Structural Chemistry of Single (S) and Double (D) Layer $M_xV_2O_5$ Phases. *J. Solid State Chem.* **1992**, *100*, 229–245.

(35) Patridge, C. J.; Wu, T.-L.; Sambandamurthy, G.; Banerjee, S. Colossal Above-Room-Temperature Metal-Insulator Switching of a Wadsley-Type Tunnel Bronze. *Chem. Commun.* **2011**, *47*, 4484.

(36) Hu, W.; Du, X.; Wu, Y.; Wang, L. Novel ε-$Cu_{0.95}V_2O_5$ Hollow Microspheres and α-CuV_2O_6 Nanograins: Facile Synthesis and Application in Lithium-Ion Batteries. *J. Power Sources* **2013**, *237*, 112–118.

(37) Parija, A.; Handy, J. V; Andrews, J. L.; Prendergast, D.; Banerjee, S. Mapping Polaronic Distortions across the Metal-Insulator Transition of Nanoscale β'-$Cu_xV_2O_5$. **2018**. Manuscript in preparation.

(38) Sethna, S. M. The Elbs Persulfate Oxidation. *Chem. Rev.* **1951**, *49*, 91–101.

(39) Galy, J.; Darriet, J.; Hagenmuller, P. Les Bronzes $Li_xV_2O_5$. Structure de La Phase β' et Affinement de La Structure de La Phase Y. *Rev. Chim. Miner.* **1971**, *8*, 509–522.

(40) Kamata, M.; Oriji, G.; Katamaya, Y.; Miura, T.; Kishi, T. Lithium Insertion Behavior of ε-$Cu_{0.9}V_2O_5$. *Solid State Ionics* **2002**, *146*, 95–100.

(41) Marshall, J. L.; Williams, P.; Rheault, J.-P.; Prochaska, T.; Allen, R. D.; Depoy, D. L. Characterization of the Reflectivity of Various Black Materials. In *Proceedings SPIE 9147, Ground-based and Airborne Instrumentation for Astronomy V*; 2014; p 91474F.

(42) Sham, T. K.; Jiang, D. T.; Coulthard, I.; Lorimer, J. W.; Feng, X. H.; Tan, K. H.; Frigo, S. P.; Rosenberg, R. A.; Houghton, D. C.; Bryskiewicz, B. Origin of Luminescence from Porous Silicon Deduced by Synchrotron-Light-Induced Optical Luminescence. *Nature* **1993**, *363*, 331–334.